X-RAY FLUORESCENCE MEASUREMENT OF IRON ACCUMULATION IN SKIN AS A SURROGATE MARKER FOR IRON LEVELS IN CRITICAL ORGANS AND TOTAL BODY IRON BURDEN

X-RAY FLUORESCENCE MEASUREMENT OF IRON ACCUMULATION IN SKIN AS A SURROGATE MARKER FOR IRON LEVELS IN CRITICAL ORGANS AND TOTAL BODY IRON BURDEN

By ERICA DAO, B.Sc.

A Thesis Submitted to the Radiation Sciences Graduate Program
and the School of Graduate Studies
of McMaster University
in Partial Fulfilment of the Requirements
for the Degree of
Master of Science

TITLE: X-Ray Fluorescence Measurement of Iron Accumulation in Skin as a Surrogate Marker for Iron Levels in Critical Organs and Total Body Iron Burden

AUTHOR: Erica Dao
B.Sc. (Honours Medical Physics)

SUPERVISOR: Dr. Michael Farquharson

COMMITTEE: Dr. Soo Hyun Byun
Dr. Bruce Wainman

NUMBER OF PAGES: ix, 80

Abstract

This thesis investigates the use of x-ray fluorescence (XRF) measurements of skin iron concentration as a non-invasive surrogate marker for total body iron burden. Rats were overloaded with iron dextran via intraperitoneal injection to investigate trends in iron accumulation in skin and organs. The skin, heart, liver, and kidney of the animals were collected and the iron concentrations were measured using the Huber XRF system and the polarized energy dispersive x-ray fluorescence (PEDXRF) system. When measured in the Huber XRF system, a very strong quadratic correlation was found between skin iron concentration and liver iron concentration (R^2=0.92). In the same system, skin iron concentration had a moderately strong linear correlation with heart and kidney iron concentration (R^2=0.53 and R^2=0.65, respectively). Measured in the PEDXRF system, heart and kidney iron concentrations were again linearly correlated with skin iron concentrations (R^2=0.34 and R^2=0.31, respectively). Liver iron concentration again showed a quadratic correlation with skin iron concentration (R^2=0.64). Therefore, it was demonstrated that skin iron concentrations can act as a surrogate marker for organ iron concentrations in rats, especially for the liver. The feasibility of using an Olympus Innov-X Delta Professional Handheld XRF Analyzer, a commercial portable x-ray fluorescence (PXRF) device, as a tool for *in vivo* skin iron analysis was investigated. The same rat skin samples measured in the previous experiment were measured using the PXRF device and compared with the organ iron concentrations as measured using the Huber XRF system. The heart and kidney showed linear correlations with skin iron concentration (R^2=0.45 and R^2=0.36, respectively). The liver showed the strongest correlation with a moderately strong quadratic correlation with R^2=0.74. It was determined that using Beam 3 in the Soil mode of this device resulted in equivalent and effective dose rates of 230±10mSv/min and 2.3±0.1mSv/min, respectively. Thus, the PXRF device has shown promise as a potential tool for measuring *in vivo* skin iron levels.

Acknowledgements

I am so incredibly grateful for having such an amazing support group throughout my studies at McMaster University. I would first like to thank Dr. Mic Farquharson for being the best supervisor ever. You put a lot of trust in your students, and that allows us to become independent thinkers and work through problems on our own. At the same time, you were always available for support and encouragement.

I would also like to thank my committee members Dr. Soo Hyun Byun and Dr. Bruce Wainman for the continued guidance throughout my project. You both are vastly knowledgeable, and your insights always led me to the correct solution (pun totally intended).

This work would not have been possible without the support of the staff at the Central Animal Facility. I would like to thank Dr. Delaney, April Scott, Tammy Robson, Mary-Ellen Cybulski, Lisa Stoa, and Jennifer Lemon for all of their assistance with my first attempts at animal care.

The peer support through the community in the graduate program has been unbelievable. Monique, Michelles, Matts, Tomas, Richard, Eric, Faraz, Peter, Alia, and Nourhan, thank you for sharing giggles, grub, and gainz. I will always hold the memories of this time close to my heart.

Immense appreciation goes to my beloved Phi. Thank you for supporting me through this entire process, especially in times of frustration and indecisiveness. Without your love, croissants, and chocolates, I would not have been able to complete this work!

Last but not least, I would like to dedicate this work to my family. Thank you to my brother Jake and Grandpa Dao for encouraging and believing in me all my life. Greatest of all, thank you to Mother Dao! You have sacrificed so much to allow me to pursue everything I am capable of in life. This is for you.

Declaration of Academic Achievement

I declare that all work submitted in this thesis is my own work and does not involve plagiarism or academic dishonesty.

I certify that I have read this thesis and that, in my opinion, it is fully adequate in scope and in quality, as a dissertation for the degree of Master of Science.

Contents

List of Figures

Chapter 1

Introduction

1.1 Iron in the Body

Iron is an essential element in normal human metabolism, playing major roles in oxygen transport, cellular respiration, and DNA synthesis[1,2]. Iron ions circulate throughout the body bound to plasma transferrin, or can accumulate in cells as ferritin[1]. Serum iron level, an indicator of circulating iron bound to transferrin, ranges between $0.55 - 1.6mg/L$ in men and $0.4 - 1.55mg/L$ in women[3]. The regulation of iron levels in the body is critical since the body does not have a physiological pathway for the removal of excess iron[1]. Both iron deficit and iron overload diseases have been observed in humans.

Figure 1.1 shows the normal iron cycle in humans. Plasma iron levels are regulated to ensure adequate iron is available to produce erythrocytes. Each day, approximately 20mg of iron, bound to transferrin, is supplied to the bone marrow for erythrocyte generation (erythropoiesis). The breakdown of erythrocytes by macrophages and iron absorbed by the gut replenishes the plasma iron supply. Duodenal enterocytes bind iron and transfer it to the plasma iron supply if sufficient iron is present, iron is stored in the enterocytes as ferritin. When these enterocytes reach the end of their life cycle, the cells are sloughed off and remove bound iron with them. This removes approximately 1-2mg of iron per day. The remaining iron is stored in the body, primarily in hepatocytes[4].

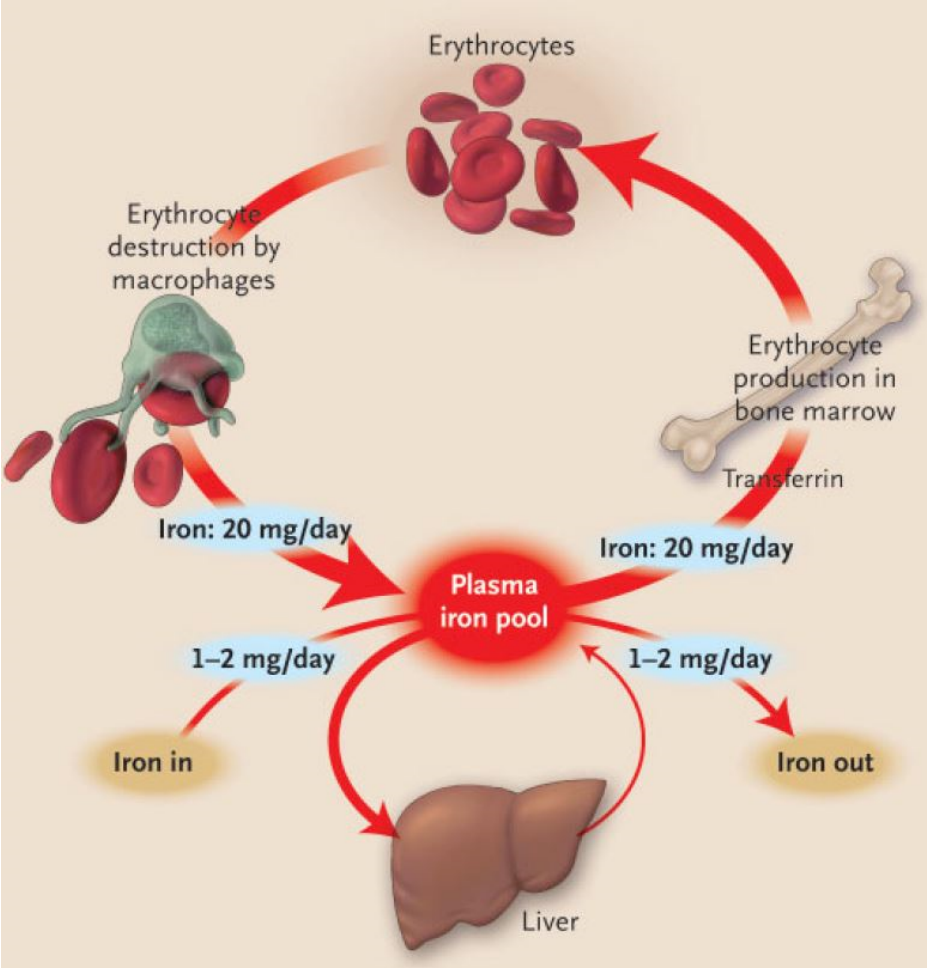

Figure 1.1: Normal iron homeostasis in humans[4].

1.2 Iron Overload Diseases

1.2.1 Hemochromatosis

Hemochromatosis is a genetic autosomal recessive disorder resulting from a mutation in the high iron (HFE) gene on chromosome 6 in humans[4]. This mutation is estimated to be carried by 1 in 9 Canadians and causes excess iron to be deposited in tissue[5]. The HFE mutation results in high plasma iron and elevated iron storage in tissues[4]. Iron overload in tissue may result in organ damage and malfunction. Hemochromatosis classically presents as diabetes, bronze pigmentation of the skin, and cirrhosis of the liver. Cardiac problems such as arrhythmias or heart failure may also arise[4]. Prognosis

of the disease and its complications is dependent on the amount and duration of the iron excess. Therefore, early diagnosis and treatment can greatly prevent adverse consequences[6,7].

The safest and most effective treatment for hemochromatosis is phlebotomy[4]. This withdrawal of blood decreases the iron levels in the blood, greatly reducing iron overload. Although established complications, such as cirrhosis or diabetes, cannot be reversed, the progression can be slowed[4].

1.2.2 Thalassemia

Thalassemia is a group of genetic autosomal recessive disorders pertaining to the defective synthesis of one or more globin proteins[8]. Incidence of thalassemia varies worldwide, but is prominent in specific locations. About 95% of affected births occur in Asian, Indian, and Middle Eastern regions[9]. There have also been recognized links to regions of the Mediterranean Sea[10]. However, changes in the epidemiology of the disease have been observed in Western populations due to increases in immigration[9]. A 2005 study found an increase in the number of patients born with thalassemia in each decade from 1960 in the Greater Toronto Area, as shown in Table 1.1.

Table 1.1: Ethnicity of and total number of patients with β-thalassemia from the greater Toronto area By decade of birth[9]

Population	<1961	1961-1970	1971-1980	1981-1990	1991-2004
Southern European (Italian, Greek), %	50	59	65.5	27.4	21.1
Middle Eastern, South Asian, Southeast Asian, %	50	41	34.5	59.6	78.9
Total No. of Patients	**24**	**39**	**55**	**62**	**71***

* Thirty-seven additional cases of homozygous β-thalassemia patients were detected by prenatal diagnosis during this time period, all from couples referred from the Greater Toronto Area.

Defective α-globin synthesis results in α-thalassemia and reduced β-globin synthesis results in β-thalassemia. Symptoms and defects vary depending on which globin genes are defective. Infants with α-thalassemia and no functional α-globin genes are stillborn or die shortly after birth[8]. People with one β-thalassemia gene are essentially in good health and have a normal lifespan[8]. However, individuals with two β-thalassemia genes suffer from anemia, ineffective erythropoiesis, and erythrocyte ruptures and

destruction (hemolysis)[8].

To combat these symptoms, patients with thalassemia often undergo regular blood transfusions. Red blood cell transfusions eliminate complications of the disease such as anemia and can extend survival[11]. Despite the success of blood transfusions in treating thalassemia, it very often results in a "second disease" of accumulation of tissue iron, which can be fatal[11]. In many instances, patients of thalassemia also undergo iron chelation therapy to reduce residual tissue iron.

1.2.3 Iron Chelation Therapy

Iron overload may cause organ malfunction or failure, resulting in death[11]. Evidence of lipid damage in iron overloaded animals and thalassemia patients have been observed[12]. Patients of iron overload diseases often undergo iron chelation therapy to remove accumulated iron in tissue. In iron chelation therapy, a chelator, with strong affinity for iron atoms, binds to and extracts iron atoms from tissue. Before chelation therapy was widely available, most chronically transfused patients died from cardiac iron failure in the first few decades of life[13]. Defaroxamine, a standard iron chelator, has been shown to dramatically improve the morbidity and mortality of these patients[11,13,14]. Chelation therapy has dramatically increased the life expectancy of iron overload patients[14]. To administer the appropriate amount of the chelator, current iron levels in tissue must be known.

1.3 Tissue Iron Measurements *in vivo*

1.3.1 Serum Ferritin Levels

A simple indirect method to assess tissue iron levels is to withdraw blood and measure serum ferritin levels. Since serum ferritin levels are correlated with iron stores in organs, tissue iron levels are estimated using known serum ferritin levels[13]. Although serum ferritin levels can reveal trends in body iron levels, serum ferritin is not a completely accurate measure of iron balance in organs[13]. Body conditions, such as inflammation or infection, can alter serum ferritin levels, therefore reducing the reliability of the reported tissue iron levels. Consequently, serum ferritin levels are poorly correlated with hepatic iron concentration in individual patients[11].

1.3.2 Biopsy

Liver biopsy is the current gold standard for the direct assessment of tissue iron content[11,13,15]. A biopsy needle is inserted into a patient and a small slender core of liver tissue is extracted. Following extraction, the iron content of the sample is accurately measured by atomic absorption spectroscopy (AAS) or other chemical or histochemical procedures[13]. However, the invasiveness of the procedure is a major limitation. Repeat biopsies are not ideal, and the procedure has an associated mortality rate of up to 0.1%[16,17].

Similarly, cardiac biopsy involves the extraction of cardiac tissue to quantify cardiac iron concentration. Safely extracting a cardiac sample is incredibly difficult; therefore, the use of cardiac biopsy as a marker for body iron burden is not the safest approach.

1.3.3 MRI & SQUID

Magnetic Resonance Imaging (MRI) is a non-invasive technique of measuring body iron levels. MRI utilizes the resonance behaviour of different atoms resulting from oscillating magnetic fields to determine iron deposition in tissues. Although MRI has been used clinically to evaluate tissue iron both *in vitro* and *in vivo*, there are significant differences between reported hepatic iron concentrations resulting from differences in equipment and methods[18,19]. Moreover, studies involving MRI to assess liver iron levels have not shown sufficient sensitivity in the iron concentration ranges found in patients with iron overload[17].

Superconducting quantum interference devices (SQUIDs) are used to measure the magnetic susceptibility of tissues to assess iron content. Magnetic susceptibility measurements have shown strong correlations with *in vitro* measurements of liver biopsy specimens[20]. A major disadvantage of this technique is that it is not widely available. There are currently only two clinical facilities with the equipment required for hepatic iron measurements[20,21].

1.3.4 Challenges

Current techniques in tissue iron measurement still face several challenges. Accurate measurement methods exist, but are quite invasive, painful, and associated with morbidity and mortality. Non-invasive measurements are either inaccurate or not

widely available. Therefore, there exists a need for a clinically available tissue iron measurement system that is both accurate and non-invasive.

1.4 X-Ray Fluorescence Measurements

1.4.1 X-Ray Fluorescence (XRF)

X-ray fluorescence (XRF) is a non-destructive interrogation technique used to determine the elemental composition of different materials. Photons incident on matter may undergo photoelectric absorption, resulting in the emission of a characteristic x-ray. By detecting these characteristic x-rays, information about the material can be determined.

An incident photon can be absorbed by inner shell bound electrons. The photon will have an energy of $h\nu$, where h is Planck's constant and ν is the photon's frequency. If the photon has an energy greater than the binding energy of that inner shell electron, E_B, that electron can be ejected from the atom. The ejected electron, now called a photoelectron, will have a kinetic energy equal to that of the incident photon energy less the binding energy of the shell from which the electron is ejected, $h\nu - E_B$. If the incident photon energy is not greater than the binding energy of the bound electron, the electron will not be ejected since there is not enough energy to release the electron from the atom.

The ejected photoelectron leaves a vacancy in the inner shell resulting in an excited atom. To de-excite, a rearrangement of electrons occurs, and this vacancy is filled by an electron from an outer shell. When an electron transitions from an outer shell to an inner shell, energy is released either in the form of a photon, known as a characteristic x-ray, or as an ejected outer shell electron, known as an Auger electron. The energy of the emitted characteristic x-ray, $h\nu'$, is equal to that of the difference between the energies of the outer shell it transitioned from and the inner shell it transitioned to. For example, Figure 1.2 shows an ejected photoelectron and an emitted characteristic x-ray from an electron transition from the L shell to the K shell.

Characteristic x-rays from different shells have different names depending on which shells they transitioned to and from. For example, a characteristic x-ray emitted from the transition from the L shell to the K shell is called a Kα characteristic x-ray. The characteristic x-rays can also be further labelled based on their transitions between subshell levels.

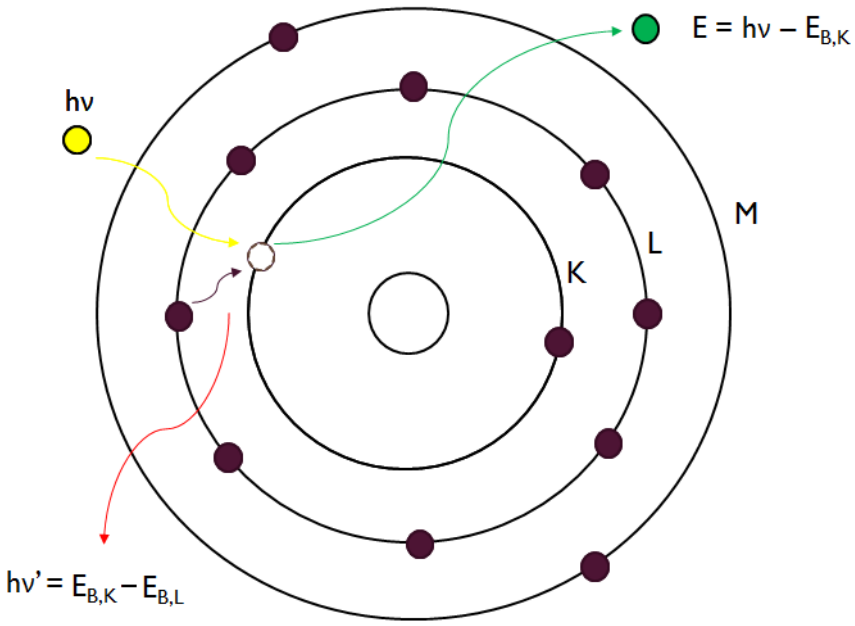

Figure 1.2: In photoelectric absorption, an incident photon (yellow) ejects a photoelectron (green). This vacancy is filled by an outer shell electron and excess energy from this transition is emitted as a characteristic x-ray (red).

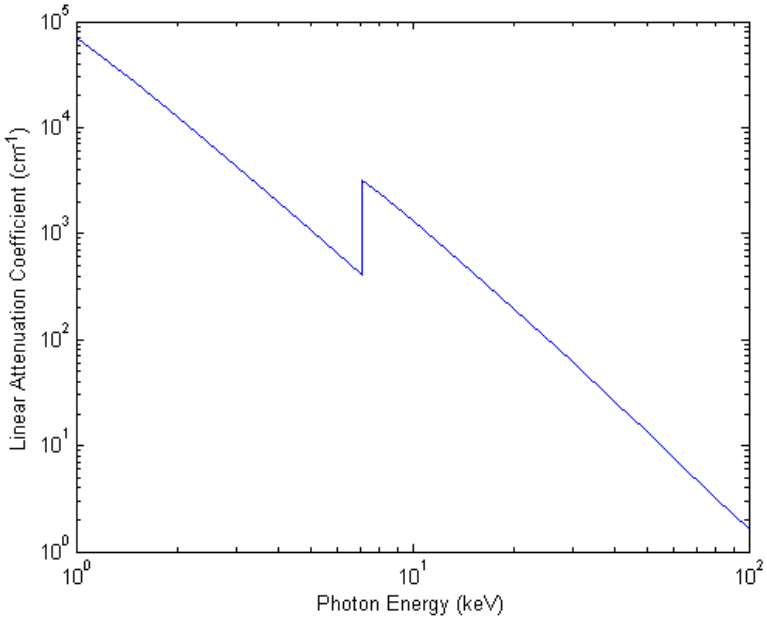

Figure 1.3: The linear attenuation coefficient of iron as a function of incident photon energy[22].

The probability of photoelectric absorption occurring is highly dependent on atomic number, approximately increasing with the cube of the atomic number (Z^3). The linear attenuation coefficient, a value that describes the extent to which a photon beam is attenuated, of iron is shown in Figure 1.3 as a function of photon energy. Photoelectric absorption is the predominant photon interaction at relatively low photon energies, decreasing in probability as energy increases. However, there is an increase in photoelectric absorption just above the electron binding energy of a shell. As a result, there is an increase in the linear attenuation coefficient just above 7.1keV, the K-shell binding energy for iron[23]. This is known as the k-edge. Therefore, to induce the greatest XRF signal from iron, an incident photon energy slightly greater than 7.1keV is ideal.

1.4.2 Skin Anatomy

The skin is a major component of the integumentary system. The primary function of this system is to enclose and protect the body from the external environment. The skin prevents internal structures from being exposed to ultraviolet radiation, bacteria, or other toxins. The skin is composed of two main layers, the epidermis and dermis. The outer epidermal layer can be further divided into five sub-layers: from superficial to deep, the stratum corneum, stratum lucidum, stratum granulosum, stratum spinosum, and stratum basale. Figure 1.4 shows the various layers of the epidermis and the dermis in human skin.

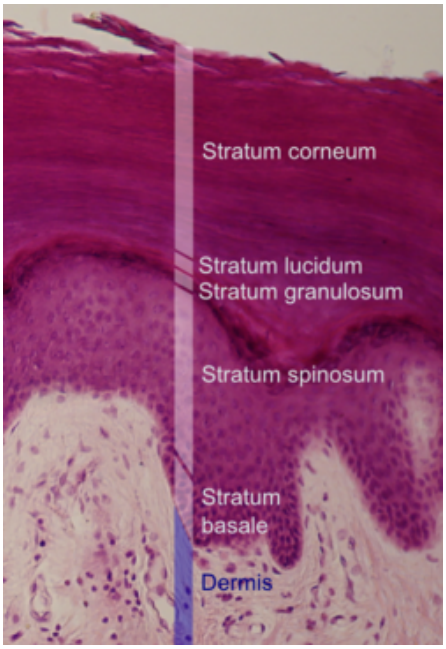

Figure 1.4: An haemotoxylin and eosin slide depicting typical skin anatomy, including the various epidermal layers[24].

1.4.3 XRF Measurements of Skin

Trace elements have been previously measured in skin using XRF[17,25,26,27,28,29,30]. Differences in elemental concentration have been observed between the epidermis and dermis for elements such as calcium (Ca), zinc (Zn), and copper (Cu). However, iron has additional differences in epidermal sub-layers. It has been observed that iron levels are greatest in the epidermal layers closest to the dermis, between the stratum granulosum to stratum basale[26,27]. The iron content then decreases towards the surface of the skin. Figure 1.5 shows a human skin sample with elemental maps shown for Ca, Zn, Fe, and Cu.

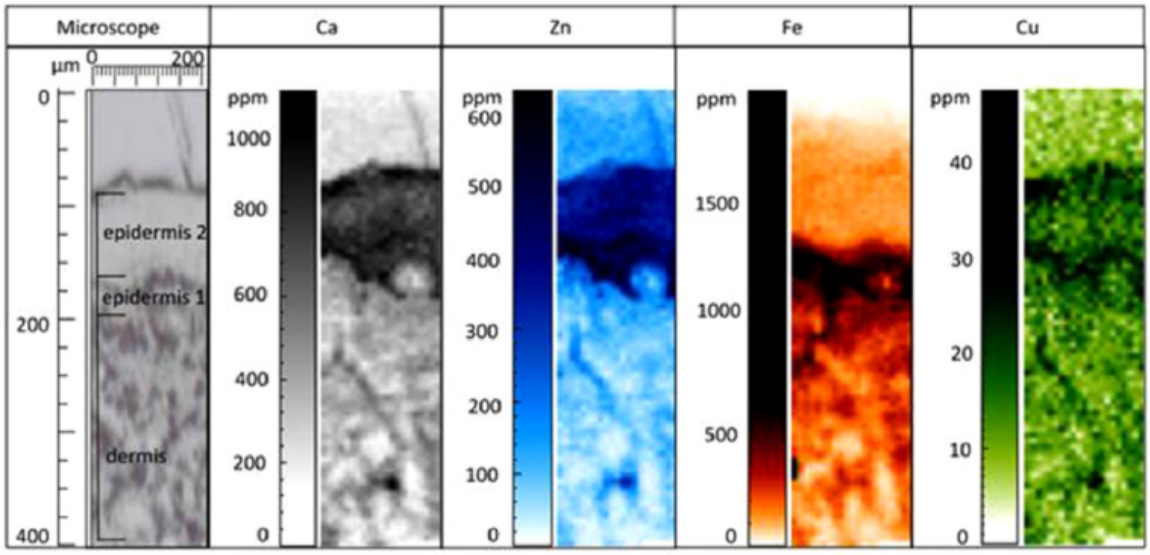

Figure 1.5: The microscope image of a skin sample and the corresponding elemental maps for Ca, Zn, Fe, and Cu[26].

This behaviour makes the quantification of iron *in vivo* a challenge. Since the epidermal thickness varies person to person, and even skin site to skin site in humans, the measured iron XRF signal may be altered. The incident photon beam may be reduced and the iron XRF signal may be attenuated on the way to the detector by the more superficial epidermal layers. Therefore, it is important to determine this thickness to calibrate any XRF devices to report concentration values in mg/kg.

1.4.4 Portable XRF Measurements

Portable x-ray fluorescence (PXRF) devices have been developed and utilized in various applications such as geology, archeometry, and soil analysis[31,32,33]. Such portable devices allow for real-time analysis in a variety of locations due to the ease of x-ray generation and detection.

Within the past few decades, the use of portable XRF devices has been investigated for feasibility for use in medical *in vivo* studies. Such studies include *in vivo* measurements of lead in bone, or arsenic and selenium in nails[34,35]. The feasibility of using these devices to measure skin has also been investigated to measure elements such as calcium, zinc, copper, arsenic, selenium, and iron[27,17,29]. Current systems have been used to measure skin phantoms or *ex vivo* skin biopsies, and there is currently no portable XRF device being used for *in vivo* skin measurements.

1.4.5 Dosimetry

When a person is exposed to radiation, energy can be deposited into the body. This energy can damage DNA, resulting in disruptions to cellular cycles or even cell death. Dosimetry is the process of measuring how much energy is deposited by ionizing radiation. Proper dosimetry allows for the characterization of the potential hazard of a certain procedure.

There are three major dose quantities: absorbed dose, equivalent dose, and effective dose. Absorbed dose is the amount of energy deposited per unit mass; it is often reported in units of Gray [Gy] where 1Gy is 1J/kg. Although absorbed dose does quantify the energy deposited, this quantity alone is not enough to assess the biological effects of radiation. The severity of the radiation dose can vary depending on the different types of radiation and the tissues or organs exposed.

A radiation weighting factor, w_r, is given to each type of radiation to account for the varying ability to produce biological effects. Table 1.2 lists the radiation weighting factor for different types of radiation. This factor is multiplied to the absorbed dose to give the equivalent dose. This dose is given the units of Sieverts [Sv] which signifies that the Gy has been multiplied by a weighting factor.

Similarly, a tissue weighting factor, w_t, is given to each tissue/organ to account for the varying sensitivities and detriment resulting from a radiation exposure. This detriment includes risk of cancer incidence, cancer mortality, life shortening, and

hereditary effects. Figure 1.6 summarizes the tissue weighting factor for various tissues/organs. This factor is multiplied to the equivalent dose to give the effective dose, which also has units of Sieverts [Sv]. Although effective dose is an accurate quantity for risk assessment, it is not quite the appropriate dose quantity for skin dosimetry. This will be further discussed in Chapter 6.

Table 1.2: Radiation weighting factors for various types of radiation[36].

Radiation Type	**Energy Range**	w_R
Photons	all	1
Electrons/Muons	all	1
Neutrons	<10 keV	5
	10 keV to 100 keV	10
	100 keV to 2 MeV	20
	2 MeV to 20 MeV	10
	>20 MeV	5
Protons	>2 MeV	5
Alpha Particles	all	20
Fission Fragments	all	20

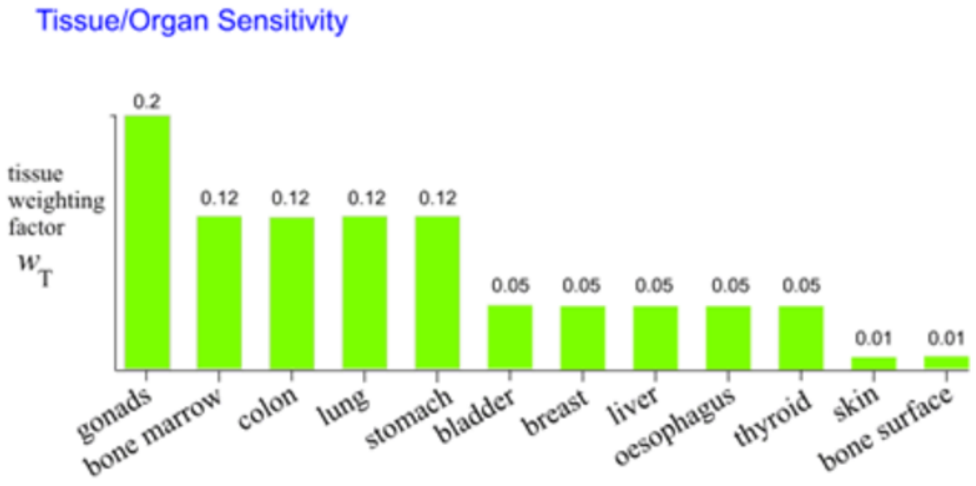

Figure 1.6: Tissue weighting factors for various types of tissues/organs[37].

1.5 Project Goal

The aim of this thesis is to determine the feasibility of using skin XRF measurements as a marker for iron levels in various organs in the body. In order to do so, this project will encompass five major experiments.

Firstly, an experiment to determine the best method of overloading rats with iron will be investigated. A comparison between ingestion of iron and injection of iron will be explored. This will be the topic of Chapter 2. Once the overload technique has been determined, experiments in overloading rats with various concentrations of iron will be performed to model iron overload disorders. Following this, the correlation between levels of iron in skin and various organs will be determined. Chapters 3 and 4 outline these experiments. In addition, XRF measurements of the skin of rats and the skin of cadavers using a portable XRF device will be discussed in Chapter 5. Finally, Chapter 6 outlines the dosimetry of using this handheld XRF device.

This thesis will outline the feasibility of using skin as a surrogate marker for iron levels in critical organs, propose the use of a portable XRF device, and discuss the dosimetry and safety of using this device in a clinical setting.

Chapter 2

Methods of Iron Overload in Rats

2.1 Chapter Outline

This chapter presents a comparison between two techniques of iron overload in rats: ingestion and injection. Iron overload experiments have been conducted previously by many different research groups either through ingestion or injection. However, there is a lack of rationale behind the selection of the method and there is currently no study that compares each technique. This study aims to quantitatively and qualitatively determine which method of overload is best.

2.2 Materials and Methods

2.2.1 Iron Overloading

Rats were selected as the animal in which iron overload would be modelled since iron toxicity in rats is more similar to iron toxicity in humans than other animals, such as mice[38]. Of the common strains of laboratory rats, albino rats were chosen since it is unknown at this time whether melanin in skin may interfere with iron measurements. The Wistar rat, a very common albino rat breed, was selected as an economical choice. Twelve male, 126-150g Wistar rats were utilized in this study. Six of these animals were in the ingestion groups, and six of these animals were in the injection group. The animals were purchased from Charles River Laboratory and housed in the Central Animal Facility at McMaster University. All animals in this study were fed standard rodent chow and drank deionized water *ad libitum*.

An iron overload solution was made by dissolving 125mg of iron (II) sulfate heptahydrate ($FeSO_4 \cdot 7H_2O$) into 100mL of deionized distilled water. This resulted in an iron (II) sulfate concentration of 1.25mg/mL. Iron (II) sulfate was selected as the iron source since it is readily available, water soluble, and previous literature has used this salt as the iron source[39,40,41]. Iron (II) sulfate has a total molecular mass of 151.92g/mol. Since iron has a molecular mass of 55.85g/mol, this means that the iron (II) sulfate is 36.76% iron. This means that the 1.25mg/mL solution of iron (II) sulfate has an iron concentration of 0.4595mg Fe^{2+}/mL.

Rats have been observed to prefer certain types of food, specifically bagels and Jell-O® (or other gelatin foods). In previous experiments, it was found that iron atoms may not be homogenous in a Jell-O® or gelatine substance since the iron may settle on the bottom as the gel sets. Therefore, bagels were selected as the food in this experiment. The ingestion groups were given 15±1g bagel pieces to eat. The three ingestion animals (Group G) had 400µL of the iron overload solution added to the bagel pieces, and the three ingestion control animals (Group GC) had only the plain bagels. These rats ate the bagels once a day, for five days a week, for four weeks in total. This resulted in Group G ingesting a total of $5 \times 400\mu L \times 4 = 8mL$ of the solution equating to a total of 10mg of iron (II) sulfate or 3.676g of Fe^{2+}. A summary of the iron overload procedure is shown in Table 2.1.

Table 2.1: The iron overload methods utilized in this 4 week study and the doses administered from the same 1.25mg/mL iron (II) sulfate solution.

Animal Group	Ingestion Group G	Ingestion Control Group GC	Injection Group J	Injection Control Group JC
n	3	3	3	3
Method	15 ± 1g Bagel Ingestion	15 ± 1g Bagel Ingestion	Intraperitoneal Injection	Intraperitoneal Injection
Volume per Dose	400µL $FeSO_4$	400µL H_2O	2mL $FeSO_4$	2mL H_2O
Frequency	5x/week	5x/week	Weekly	Weekly
Total Volume Adminstered	8mL	8mL	8mL	8mL
Total Dose Adminstered	3.676mg Fe^{2+}	0mg Fe^{2+}	3.676mg Fe^{2+}	0mg Fe^{2+}

The six rats in the injection groups were injected intraperitoneally. The three injection animals (Group J) were injected with 2mL of the iron solution and the three injection control animals (Group JC) were injected with 2mL of deionized water. These rats were injected once a week for four weeks. This resulted in Group J receiving a total of $4 \times 2\text{mL} = 8\text{mL}$ of the iron solution equating to a total of 10mg of iron (II) sulfate or 3.676g of Fe^{2+}. The injection groups were then given a 4 week equilibriation period where they were no longer receiving any injections.

Designed in this way, both Groups G and J received the same total volume made from the same solution. It can then be assumed that each animal received the same total dose. The overloaded animals in this study received 10mg of iron sulfate. Assuming the animals had a weight of 125g, this meant the animals received a dosage of 80mg/kg of iron sulfate, or approximately 30mg Fe^{2+}/kg. Previous iron overload studies suggest that this value should result in measurable iron accumulation without significant negative health effects[42].

Following overloading, organs and skin were collected from each of the animals. Organs collected were heart (H) and liver (Lv). The heart and liver are of significant clinical importance, with evidence of iron accumulation found in literature. Five skin samples were biopsied from each animal from a variety of sites: top of the head between the ears (T), left side of abdomen (LA), right side of abdomen (RA), upper back (UB), and lower back(LB). Each biopsy was 8mm in diameter.

The naming convention used was a string composed of the group the animal was from (G, GC, J, or JC), the animal number (1, 2, or 3), and lastly the sample site (H, Lv, T, LA, RA, UB, or LB). For example, a sample of the ingestion control group from the first animal from the left abdomen skin site would be named GC1LA.

2.2.2 XRF Measurements

2.2.2.1 Ingestion Groups

The ingestion groups measurements were obtained at the FLUO beamline at the Angstromquelle Karlsruhe(ANKA) synchrotron facility in Karlsruhe, Germany. Five samples from each of the six animals from Groups G and GC were measured, totalling 30 samples. Due to a limited schedule at the facility, measurements of all samples from all animals was not possible. The heart and liver was measured for all six animals and three of the five skin sites were measured from each animal. The skin sites were

selected to ensure comparisons between the groups was possible.

The sample were cryogenically sectioned to be mounted onto slides. The samples were frozen in Tissue-Tek Optimum Cutting Temperature (OCT) Compound to hold in place as the samples were microtomed to produce 50µm thick slices. The slices were then placed on sample frames composed of polyethylene and Ultralene® XRF film. The samples were then preserved by freeze drying for 1.5 hours. The finished samples can be seen in Figure 2.1. The normally clear and colourless OCT compound becomes opaque and white when frozen, and remains this colour following freeze drying.

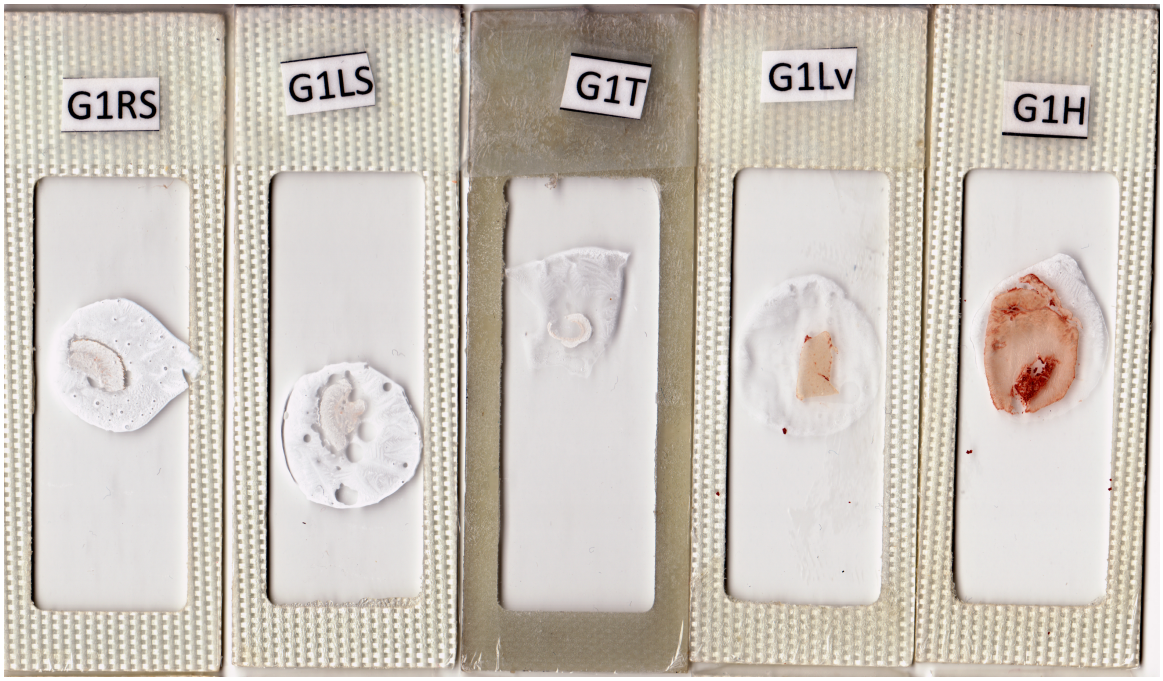

Figure 2.1: The freeze dried sample slides with 50µm thick embedded in the OCT compound.

At the ANKA facility, the samples were placed at a 45° angle on a stage with three degrees of freedom for movement in all three planes. Incident on the sample was a focussed 8keV synchrotron beam, and the XRF response was measured using a silicon drift detector at 90° from the incident beam. This experimental setup is shown in Figure 2.2.

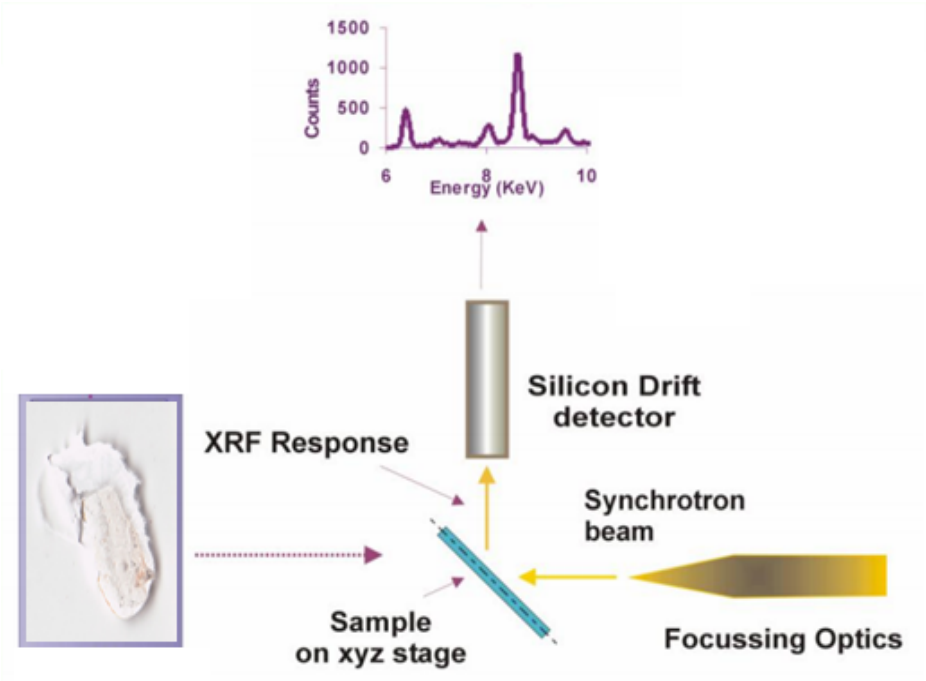

Figure 2.2: The experimental setup used to measure Groups G and GC at the ANKA synchrotron facility[26].

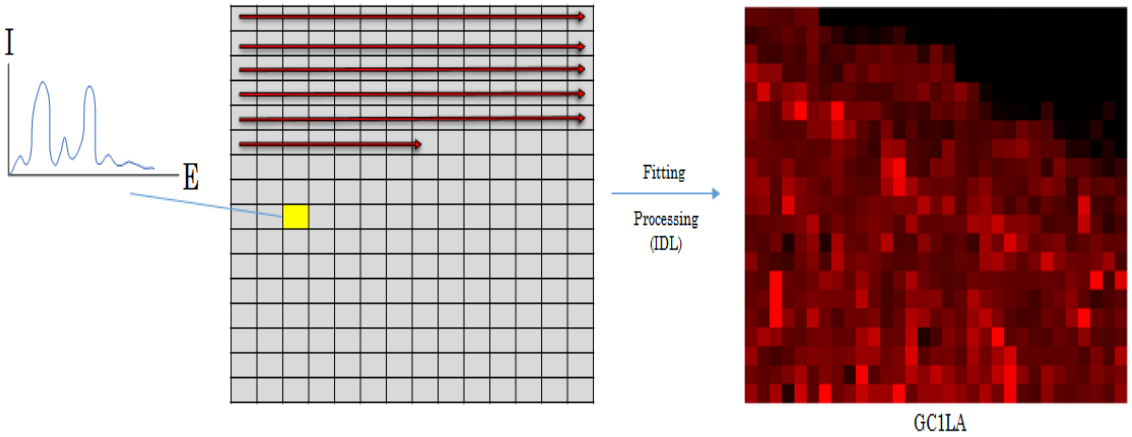

Figure 2.3: The raster scanning, peak fitting, and processing of sample GC1LA. The red-to-black pixel gradient indicates the concentration gradient from high concentration-to-low concentration.

The $20\mu m \times 20\mu m$ beam measured the XRF response of a single spot on the sample. The sample was moved on the sample stage, first all along the x-axis and then along the y-axis, to measure the XRF response in a larger region. This technique is known as raster scanning. Each measured XRF response was collected for 1s before moving on to the next pixel. Once an x-ray spectrum was collected for each point, the integral area under the iron Kα and argon Kα peaks were determined by peak fitting using PyMCA. The integral peak area for iron was normalized to argon to account for small differences in sample distance to detector since argon is found in air. This also allows for comparison of the values measured on different detectors. This normalized integral area can be considered a concentration value, in arbitrary units. Following normalization, IDL was used to sort the data and produce an image of the area scanned. Figure 2.3 depicts this process.

With the very focussed and small beam available at the ANKA facility, maps depicting the concentrations in a chosen region could be determined. This level of detail will enable analysis on a small scale, and trends in the distributions of iron can be determined.

2.2.2.2 Injection Groups

The injection group samples were prepared in the same manner as the ingestion group samples as outlined in Section 2.2.2.1. The injection groups measurements were obtained at the VESPERS beamline a the Canadian Light Source synchrotron facility in Saskatoon, Saskatchewan. Similarly, 30 samples were measured. Heart, liver, upper back, lower back, and center abdomen samples were measured for all 6 animals of Groups J and JC. The samples were measured with the same geometry, however, the detector used was a four element Vortex detector. A few other differences include a beam size of 10µm×10µm and each pixel was measured for 15s.

2.3 Results & Discussion

2.3.1 Ingestion Groups

Accumulation comparisons will be made by comparing the iron content of samples from each group. Heart, liver, and skin from the top of the head was measured for all 6 animals in the ingestion study. The iron content was determined by averaging

the normalized iron peak area of each pixel in the image. The mean concentration (arbitrary units) for each sample, and the mean iron concentration for an entire group (three samples per group) were calculated. The standard error of the means was calculated using the following equation:

$$s = \sqrt{\frac{\Sigma(x - \bar{x})^2}{n - 1}} \tag{2.1}$$

Table 2.2: The sample mean iron concentration (arbitrary units), group mean iron concentration and the corresponding standard errors for the heart, liver, and skin from the top of the head samples of Groups GC and G.

Heart Sample	Mean Iron $\times 10^{-3}$	Standard Error $\times 10^{-3}$	Group Mean Iron $\times 10^{-3}$	Standard Error $\times 10^{-3}$
GC1H	14.1	0.1		
GC2H	13.4	0.1	14	3
GC3H	13.5	0.1		
G1H	14.6	0.1		
G2H	13.6	0.1	14	2
G3H	14.0	0.1		
Liver Sample	Mean Iron $\times 10^{-3}$	Standard Error $\times 10^{-3}$	Group Mean Iron $\times 10^{-3}$	Standard Error $\times 10^{-3}$
GC1Lv	25.7	0.2		
GC2Lv	25.7	0.3	28	9
GC3Lv	33.3	0.3		
G1Lv	28.9	0.4		
G2Lv	33.1	0.3	31	7
G3Lv	32.0	0.5		
Skin (T) Sample	Mean Iron $\times 10^{-3}$	Standard Error $\times 10^{-3}$	Group Mean Iron $\times 10^{-3}$	Standard Error $\times 10^{-3}$
GC1T	4.6	0.1		
GC2T	2.16	0.04	3	1
GC3T	2.62	0.04		
G1T	3.66	0.07		
G2T	3.01	0.06	3	1
G3T	1.90	0.04		

A summary of the sample means, group means, and standard errors can be found

in Table 2.2. It can be seen that the mean iron content of each group is not different between Groups G and GC. However, a Mann-Whitney-u significance test was performed on the iron content of each pixel in animals of Group G and the iron content of each pixel in animals of Group GC. Significant differences were found for the heart, liver, and skin from the top of the head, $p=0.001$, $p<0.001$, and $p<0.001$, respectively. Statistical analysis was performed using the IBM SPSS software.

So, it appears that although the mean iron content of a sample is the same, the distribution of iron content in each sample group is different. This can be seen in the histogram of the pixel values within a sample. Histograms for skin samples for one animal in the ingestion group and one animal in the control group are shown in Figure 2.4. It can be seen that most of the pixel values in the ingestion group are higher than most of the pixel values in the control group. However, the mean of each sample is quite similar. Upon inspection of all samples and sample sites in this manner, and through the Mann-Whitney-u significance test, it can be concluded that the ingestion group did have a higher iron content than the control groups for the heart, liver, and skin sites.

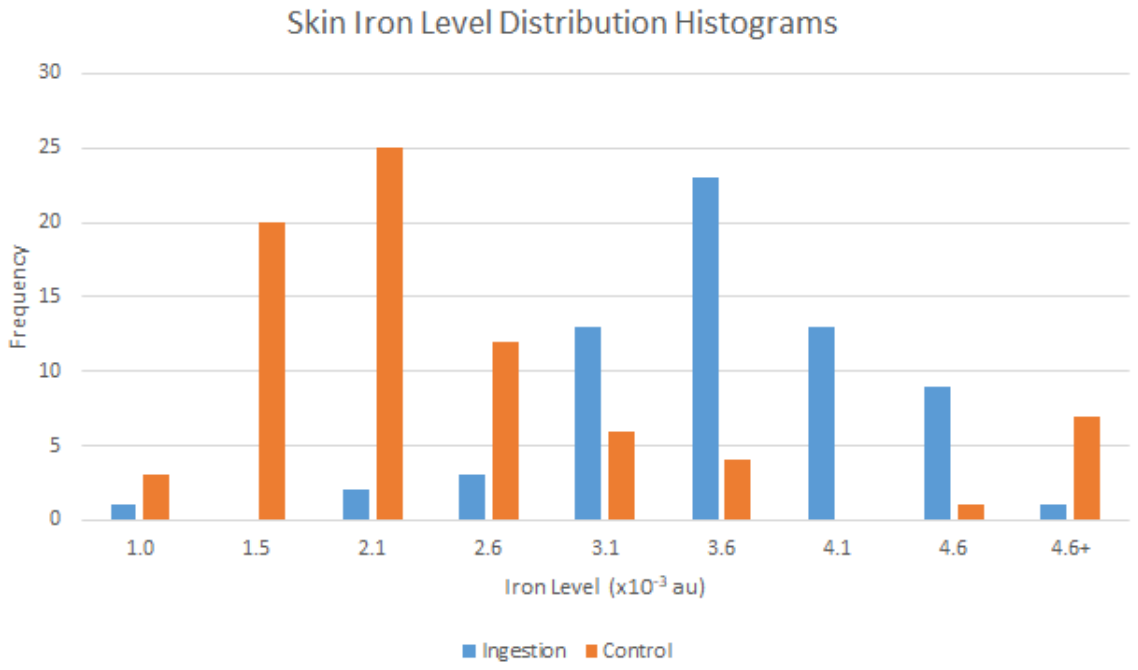

Figure 2.4: A histogram of the iron concentration for each pixel within an ingestion and control sample.

2.3.2 Injection Groups

The same analysis was performed on the animals in the injection groups. The mean iron concentration and associated standard error for the injection and injection control groups for the heart, liver, skin from upper back, skin from lower back, and skin from left abdomen is shown in Table 2.3. Again, there were 3 animals in each group. Statistically significant increases in iron concentration in the injection group were observed in all organs and skin; Mann-Whitney-u significance test values were $p=0.017$ for the heart and $p<0.001$ for the liver and all skin sites.

Table 2.3: The group mean iron concentration (arbitrary units) and the corresponding standard errors for the heart, liver, and skin samples for Groups JC and J. There were 3 animals in each group.

Heart	Group Mean Iron $\times 10^{-3}$	Standard Error $\times 10^{-3}$
Control	18.9	0.3
Injection	19.8	0.2
Liver	Group Mean Iron $\times 10^{-3}$	Standard Error $\times 10^{-3}$
Control	42.1	0.5
Injection	45.6	0.6
Skin from Left Abdomen	Group Mean Iron $\times 10^{-3}$	Standard Error $\times 10^{-3}$
Control	2.3	0.2
Injection	2.7	0.2
Skin from Upper Back	Group Mean Iron $\times 10^{-3}$	Standard Error $\times 10^{-3}$
Control	2.1	0.2
Injection	3.0	0.2
Skin from Lower Back	Group Mean Iron $\times 10^{-3}$	Standard Error $\times 10^{-3}$
Control	2.7	0.2
Injection	2.9	0.1

2.3.3 Iron Distribution

It has been observed that the iron concentration measured is not homogeneous throughout the skin. For most of the samples, a distinct increase in iron accumulation can be measured approximately 60-180μm below the stratum corneum. Figure 2.5 shows two

examples of skin samples where a distinct band can be observed. This phenomenon was observed in rats from all groups, regardless of iron overload treatment. Previous studies have shown that there is an accumulation of iron at the boundary between the epidermis and dermis, most likely in the stratum granulosum or stratum basale, in human skin[26]. It has been previously reported that this pattern is unique to iron; this trend was not observed for copper, zinc, or calcium in human skin. The observation in this experiment demonstrates that this phenomenon can also be observed in the skin of rats, suggesting that rat skin can appropriately be used as a model for human skin.

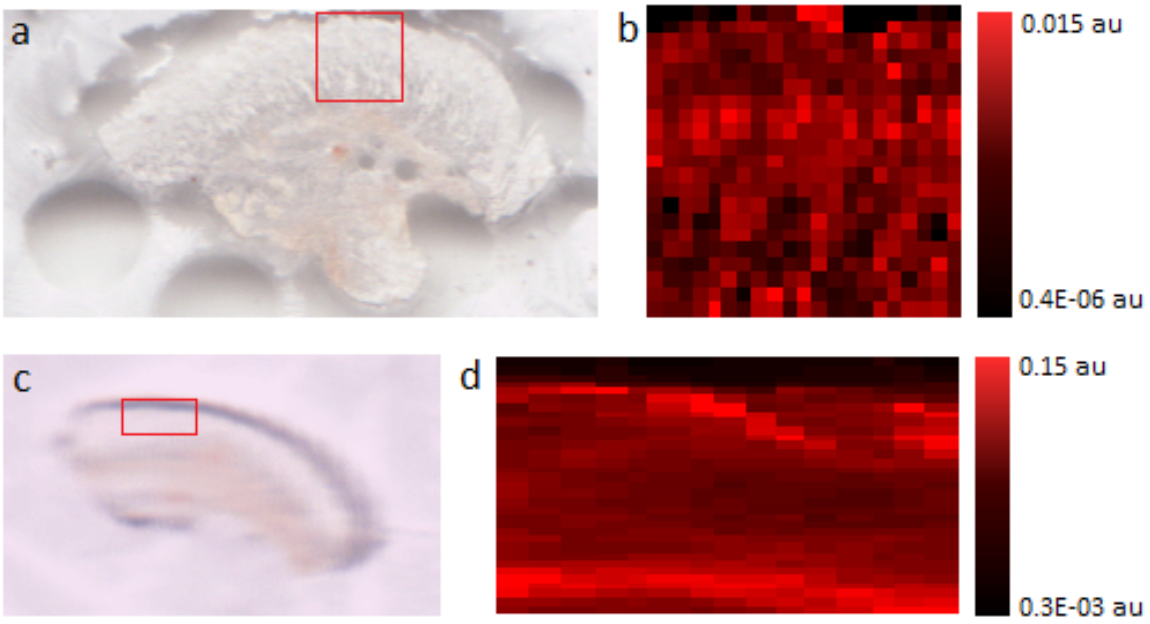

Figure 2.5: Images of skin samples. The red inset outlines the area scanned and the corresponding iron concentration. a) Image of the G1LA skin sample. b) The iron concentration distribution map for the area outlined in the G1LA sample. A distinct band can be observed in the middle of the distribution map. c) Image of the JC2LB skin sample. d) The iron concentration distribution map for the area outlined in the JC2LB sample. A distinct band can be observed near the bottom of the distribution map.

2.3.4 Ingestion vs. Injection

Although both groups showed statistically significant increases in iron, suggesting that the iron overload was successful, only the injection group showed discernible differences in the mean of the overload and control groups. The following chapter will present a

new experiment conducted using a different system, with a larger beam size. The new measurement system will be measuring bulk tissue, where only the mean value of the area is measured, with no spatial discrimination. Since injection showed greater iron accumulation with the same overload dose, it has proven to be the superior method of iron overload.

In addition, injection of an iron solution was a more efficient method than ingestion in execution. When giving the bagel pieces to the animals to eat, the animals had to be actively monitored to ensure that the entire piece was ingested and the entire dose was administered. This was quite time intensive since the animals were easily distracted. Ensuring that each piece was fully eaten took up to 20 minutes per animal. In contrast, the injection method was much quicker, taking approximately 5 minutes per animal.

2.4 Conclusion

In this experiment, two iron overload techniques were administered to investigate iron accumulation in the heart, liver, and skin of rats. It was shown that both the ingestion and injection of iron would result in iron overload; however the extent to which this overload can be observed varied. The animals that ingested iron sulfate showed a statistically significant increase in iron when examined on a micrometer scale, but the average iron concentration within a sample was not much higher than the control animals. This suggests that although there was iron accumulation, bulk tissue measurements using larger beam sizes would not result in measurable differences. The animals that were injected with the iron sulfate solution also displayed statistically significant increases in iron accumulation, and greater accumulation overall. This resulted in mean sample iron concentration values that were more distinct than those of the control animals. Finally, since rat skin mimics the iron distribution patterns previously found in human skin, it can be concluded that the skin of rats can appropriately be used to model the characteristics of human skin. A shortcoming of this study was that the dose administered was quite low, and therefore further studies are needed at higher doses to fully investigate the effectiveness of overloading rats with iron.

Chapter 3

Preliminary Iron Overload Study

3.1 Chapter Outline

This chapter reports the findings of a new experiment using a new iron solution and a higher dose compared to that of the previous experiment outlined in Chapter 2. The iron uptake for two dosages will be reported, and the effect of dose administration frequency will be investigated.

3.2 Materials and Methods

3.2.1 Iron Overloading

In this experiment, male Wistar rats weighing 126-150g were injected with varying amounts of an iron dextran solution. The iron solution was changed from iron (II) sulfate to iron dextran since iron dextran has greater clinical presence and is commonly used for treating anemic animals. Anem-X injectable iron dextran of 100mg of Fe^{2+}/mL concentration was used in this study. The same iron dextran solution was used for all animals, but the volume of the same solution was varied to administer different doses.

The six rats of Group A were injected once a week with deionized water to act as the control. Group B consisted of six rats that received weekly injections of 0.2mL of the iron dextran solution and Group C consisted of six rats that received weekly injections of 0.4mL of the iron dextran solution. These animals received 20 and 40mg Fe^{2+} per week, respectively. This is more than six and ten times greater than the doses of the animals in the previous experiment. To study the effect of injection frequency,

the six rats in Group D were injected with 0.2mL of the iron dextran solution twice a week, resulting in a dose of 40mg Fe^{2+} each week. This means that Group C and Group D received the same total amount of dose each week. The animals were injected for four total weeks and given an 8 day equilibriation period. Table 3.1 summarizes the animal groups. All animals were fed standard rodent chow and drank deionized water *ad libitum*.

Table 3.1: The iron overload method utilized in this 4 week study and the total doses administered.

Group	Group A	Group B	Group C	Group D
n	6	6	6	6
Volume per Dose	0.2mL H_2O	0.2mL Iron Dextran	0.4mL Iron Dextran	0.2mL Iron Dextran
Frequency	Weekly	Weekly	Weekly	2x/week
Total Volume Adminstered	0.8mL	0.8mL	1.6mL	1.6mL
Total Dose Adminstered	0mg Fe^{2+}	80mg Fe^{2+}	160mg Fe^{2+}	160mg Fe^{2+}

Organs and skin were collected from each of the animals. The heart (H), liver (Lv), kidney (K), and spleen (Sp) were collected from each animal. The heart and liver are of significant clinical importance, with evidence of iron accumulation found in literature. The kidney and spleen were selected as organs to compare iron accumulation since there has been little to no evidence of iron accumulation in these organs in iron overload. Four 8mm skin biopsies were extracted from each animal from a variety of sites: top of the head between the ears (T), abdomen (A), upper back (UB), and lower back (LB). Varied sites were selected to investigate possible location dependence in iron accumulation.

A similar naming convention to that of the previous experiment was used. The sample name was a string composed of the group the animal was from (A, B, C, or D), the animal number (between 1-6), and lastly the sample site (H, Lv, K, Sp, T, A, UB, or LB). For example, a sample from the control group from the first animal from the lower back skin site would be named A1LB.

3.2.2 XRF Measurements

All samples were measured in the Huber X-Ray Fluorescence (XRF) Measurement System at McMaster University. The Huber is a bulk tissue measurement system. In order to be measured, the samples had to be mounted in a specific manner. The samples were placed into 25.4mm wide sample holders, filling a cylindrical volume that was 12.7mm in diameter and 1mm thick. The samples were then covered on both sides with ultralene x-ray film. An example of the sample holder is shown in Figure 3.1. The sample holders are then placed onto a sample mount angled at 45°. The sample mount is shown in Figure 3.2. A small peg is inserted through the small hole near the bottom of the sample holder and through the hole in the sample mount to keep the sample position locked during measurement.

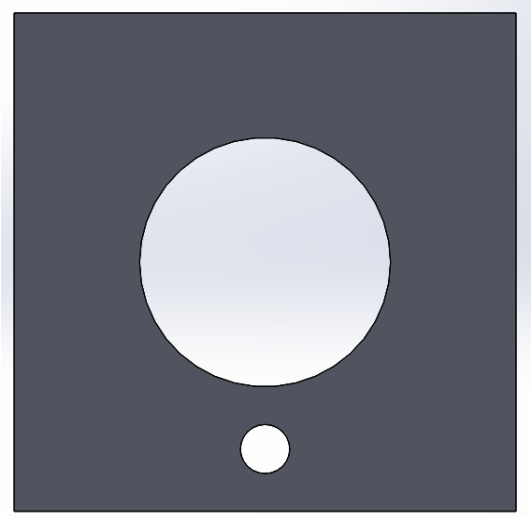

Figure 3.1: The samples filled the hole in the center of the holder.

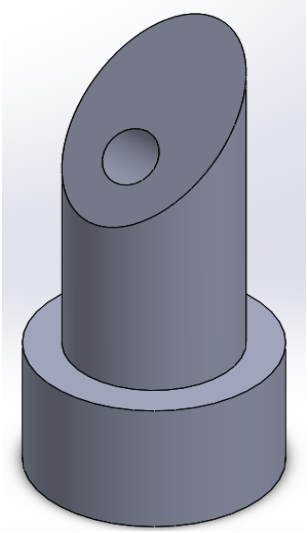

Figure 3.2: The sample holder is held into place on this mount using a peg.

A 2mm×2mm beam was incident on the center of the sample holder and the x-ray emission is detected with a silicon drift detector which is 90° from the sample. This geometry is similar to that used at the synchrotron facilities, but the beam size is larger. The x-ray tube was operated at 50kV and 500µA.

All heart, liver, kidney, spleen, skin from top of head, skin from abdomen, skin from upper back, and skin from lower back samples of each animal were measured. An x-ray spectrum was collected for 1 hour for each sample. Eight samples, one from each organ/skin site, were measured three times within the same sample holder to check for homogeneity. These samples were measured in the center of the sample,

then the sample stage was moved vertically 2mm below and vertically 2mm above the center. Since the sample was angled at 45°, this 2mm change resulted in a $\frac{2}{sin(45°)}$mm (approximately 2.8mm) distance between the sampled points. Each of these points was also measured for one hour. Figure 3.3 depicts the different areas measured within the same sample.

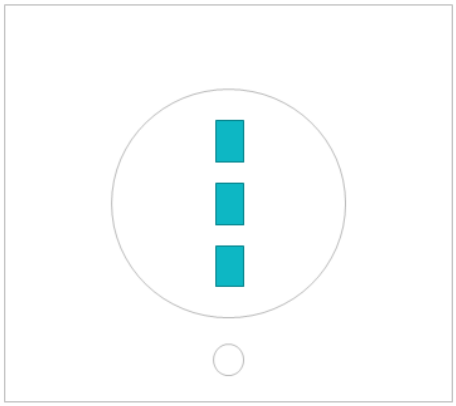

Figure 3.3: The three different areas measured within the same sample. The center of each beam is approximately 2.8mm apart.

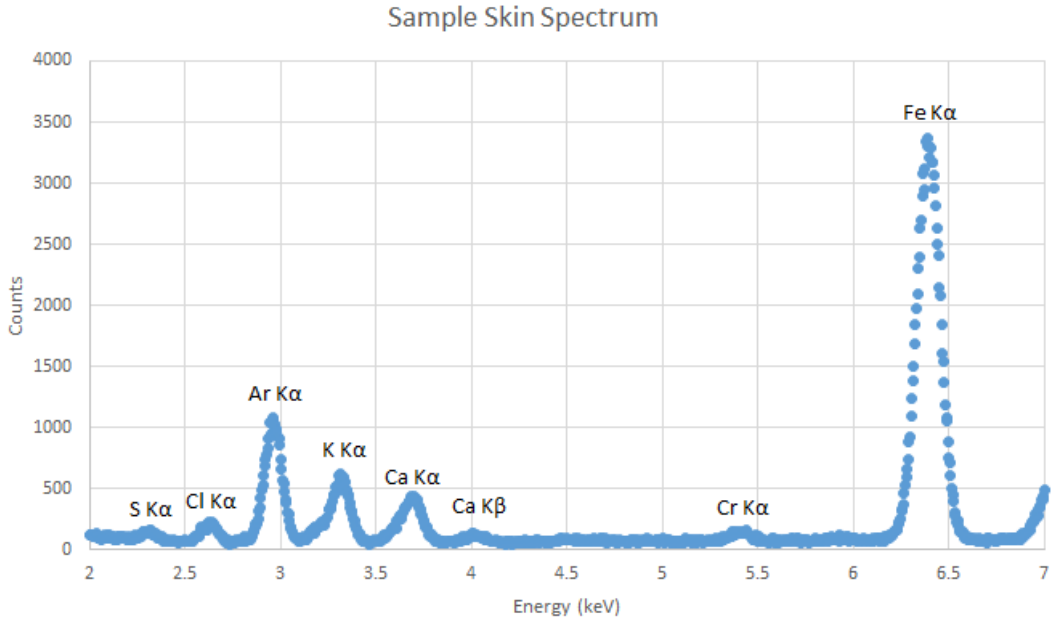

Figure 3.4: A sample spectrum from a skin sample indicating the argon (Ar) and iron (Fe) Kα peaks.

Figure 3.4 shows a sample spectrum from a skin sample with labels for the argon Kα and iron Kα peaks indicated. From the collected spectra, the integral peak areas for the iron Kα and argon Kα peaks were determined using the PeakFit software. The iron peak area was normalized to the argon peak area to report the iron concentration value of the sample in arbitrary units. Statistical analysis was performed using the IBM SPSS software.

3.3 Results & Discussion

3.3.1 General Results

During overloading, three animals died prior to the end of the experiment. After the third week of injections, one animal from Group B and one animal from Group C died unexpectedly. At this point in time, the animal from Group B had received 60mg of Fe^{2+} and the animal from Group D had received 120mg of Fe^{2+}. The animal from Group C was sent to pathology to determine cause of death. The pathology report concluded that the animal had died from septicemia induced by rapid decline in the immune status, pleurititis, pericarditis, and periostitis all resulting from iron overload. The animal from Group B was not sent for pathology and samples were still collected from this body.

Following the fourth and final week of injections, another animal from Group C died. This animal had received the full 160mg of Fe^{2+}. Since the cause of death was concluded to be as a result of iron overload, this animal was not sent to pathology and the samples were still collected. In total, samples were collected for 23 of the original 24 animals.

Figure 3.5 shows sample spectra for the abdominal skin for one animal in each of the groups and the measured background of an empty sample holder. It can be seen that all of the animals have higher iron peaks than background. In addition, the animals overloaded with iron have higher iron peaks than that of Group A, the control group. Groups C and D have iron peaks that are similar, and both are higher than Group B.

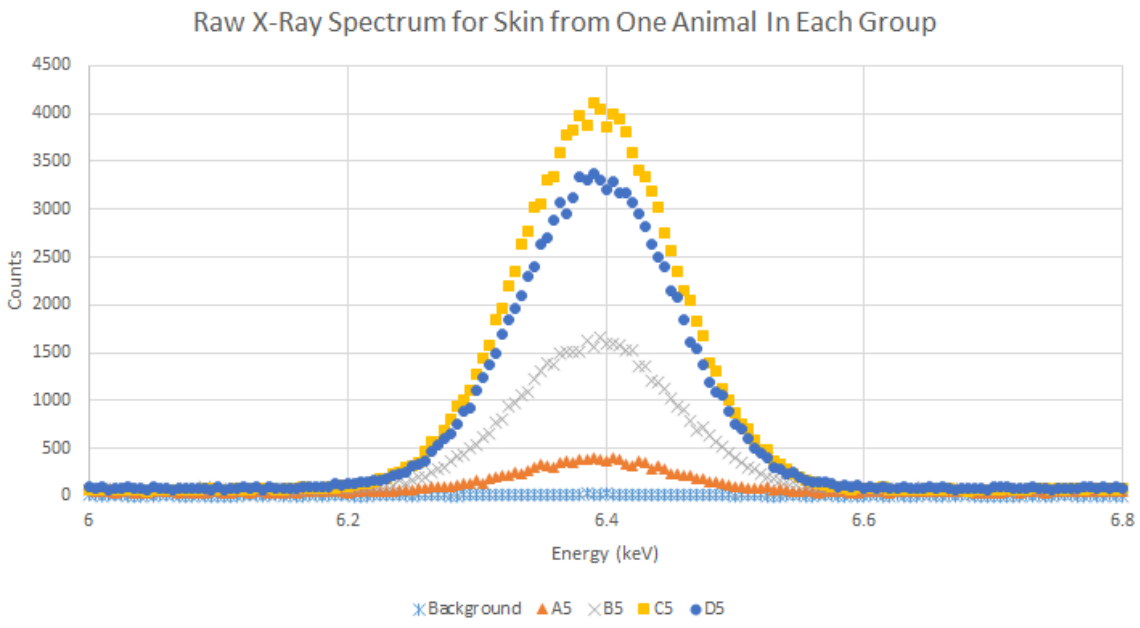

Figure 3.5: Sample spectra from the abdominal skin for one animal in each group and background.

3.3.2 Organs

To determine whether iron had accumulated in different organs, the iron concentrations of the samples in each group were compared. Figure 3.6 shows boxplots for the iron concentration for each organ.

For the heart, the control animals from Group A had the lowest amount of iron. It was found that there was a statistically significant increase in iron in Group B compared to Group A ($p<0.01$) and an increase in iron in Group C and D compared to Group A ($p<0.01$ for both). For a 95% confidence interval, there was a statistically significant difference between Groups B and C ($p=0.05$). There was no difference found between Groups C and D, suggesting that the iron accumulation in the heart is not dependent on dose administration frequency. For the liver, kidney, and spleen, there was a statistically significant increase in iron in the animals of Groups B, C, and D compared to Group A ($p>0.01$ for all). There was no difference found between the animals of Groups B, C, or D in these organs.

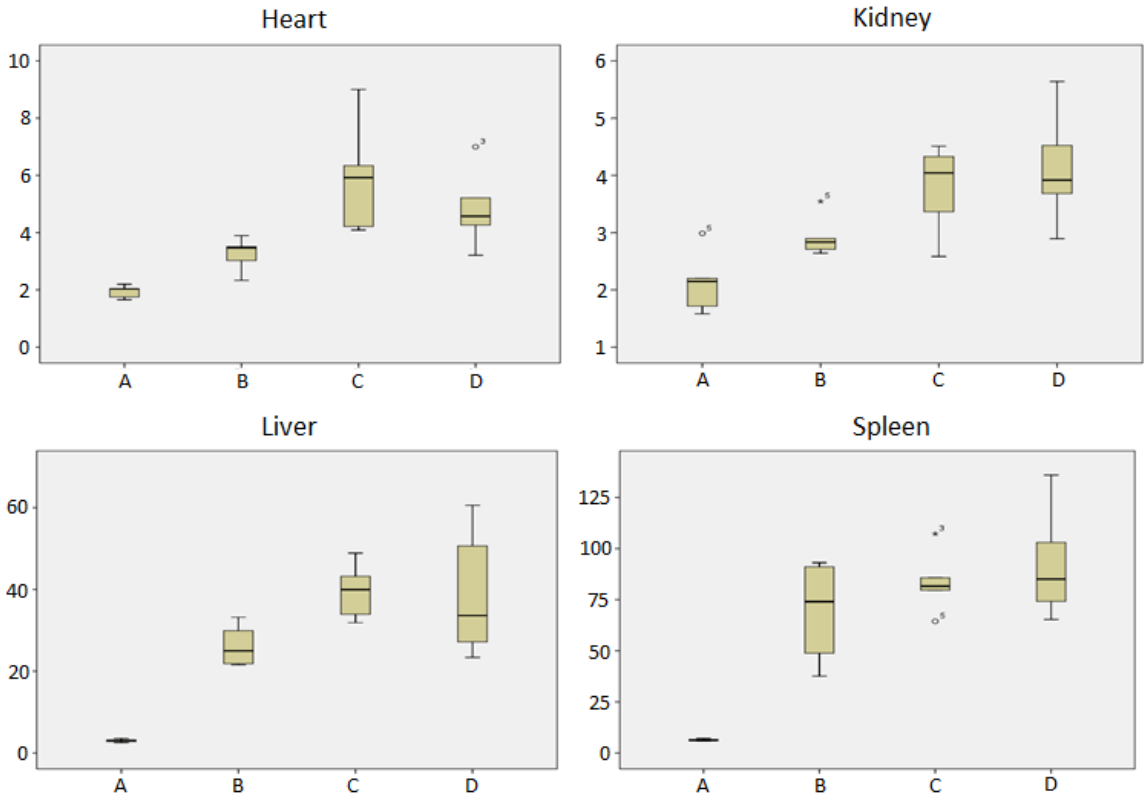

Figure 3.6: Boxplots of the iron concentrations, in arbitrary units, of the heart, kidney, liver, and spleen for each group.

This shows that rats that are injected with iron do accumulate iron in their organs; however the uptake of each individual animal is different. Therefore, it is not reasonable to group animals together for analysis since different animals may have accumulated different fractions of the total administered dose. From Figure 3.6, it can be seen that the range of iron concentrations for the overloaded animals is much greater than that of the control animals so it is confirmed that at least some of the injected iron accumulates in the organs.

3.3.3 Skin

Figure 3.7 shows boxplots for the iron concentration in various skin sites. There were statistically significant increases in iron for all skin sites in the groups that received the iron injections compared to the control animals of Group A ($p<0.01$ for all). There was an increase in iron between Groups A and B for all skin sites ($p<0.01$ for all).

There was an increase in iron between Groups B and C for the skin from the top of the head and abdomen ($p<0.01$ for both); however there was no difference found for the skin of the lower and upper back for these groups. There was no difference in iron between Groups C and D for any of the skin sites, again suggesting that there is no dependence on dose administration frequency.

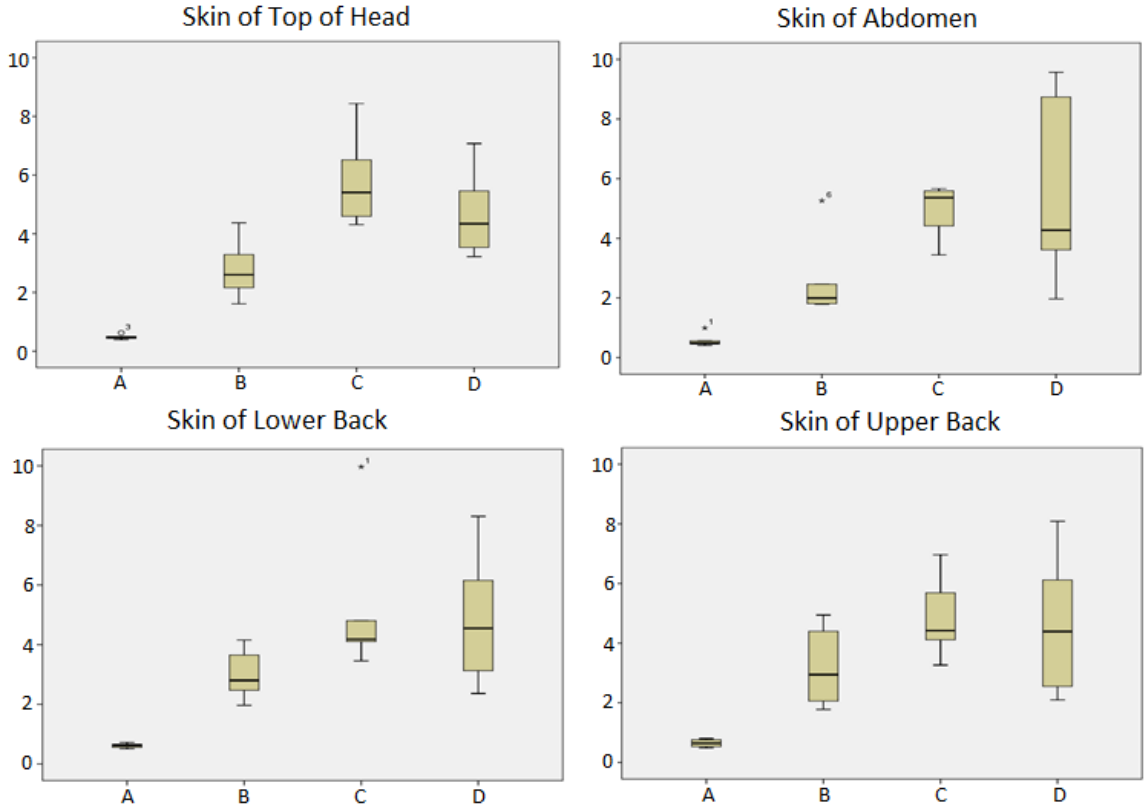

Figure 3.7: Boxplots of the iron concentrations, in arbitrary units, of the skin from the top of the head, abdomen, lower back, and upper back.

Analysis was conducted to determine if there were differences between the various sites. Figure 3.8 shows boxplots for the iron concentrations for each site within a group. There was no difference found between the skin sites in each group: $p=0.333$ for Group A, $p=0.545$ for Group B, $p=0.674$ for Group C, and $p=0.931$ for Group D. This suggests that sampling any of the skin sites of an animal is sufficient.

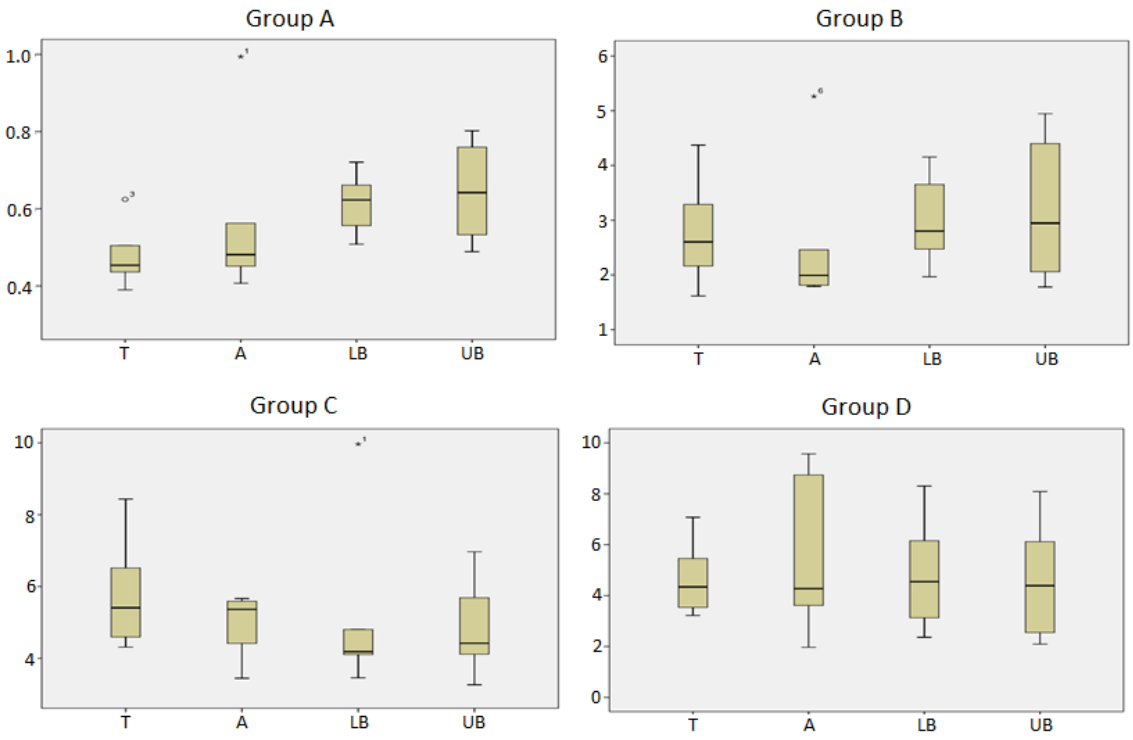

Figure 3.8: Boxplots of the iron concentrations, in arbitrary units, of each skin site for each group.

Figure 3.9 shows boxplots for the iron concentrations for all of the skin sites in each group. When grouped, it can be seen that there is a significant increase in iron between Groups B, C, and D compared to Group A ($p<0.01$ for all). In addition, there was an increase in iron between Groups C and D, and B ($p<0.01$ for both). However, where was no difference between Groups C and D. This suggests that there is no dependency on when the dose is administered.

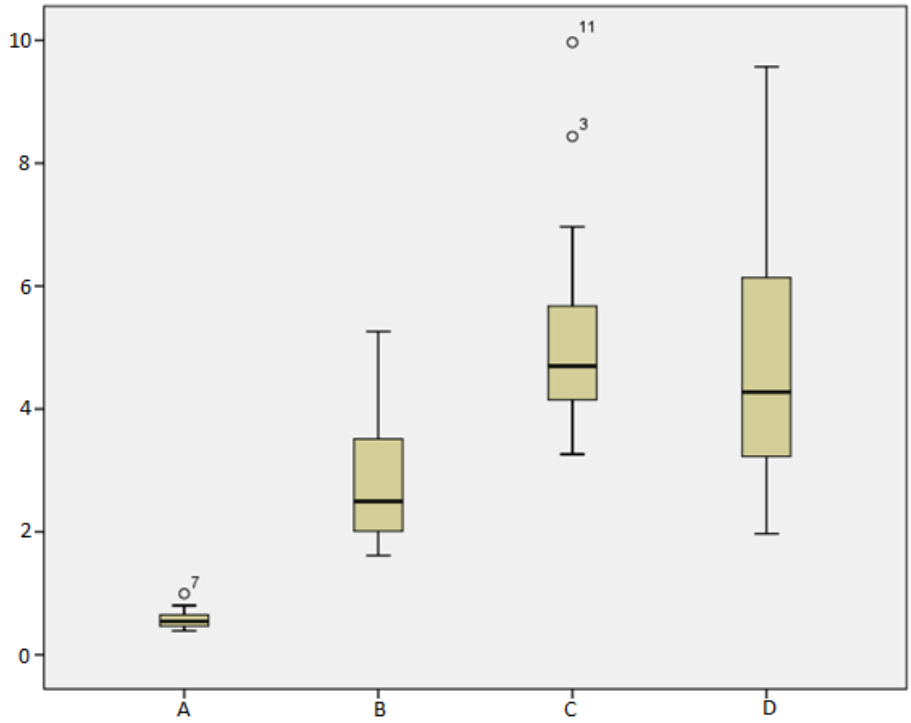

Figure 3.9: Boxplots of the skin iron concentrations, in arbitrary units, for all skin sites for all animals in each group.

3.3.4 Correlation between Organs and Skin

Figure 3.10 shows the heart iron concentration plotted with skin iron concentration for all 23 animals in the study. The errors on the concentration values are the result of two uncertainties summed in quadrature; the counting error, the square root of the counts following a Poisson distribution; and the fitting error, the standard error between the data points and the peak of best fit.

It can be seen that there is a correlation between the heart iron concentration and the skin iron concentration with R^2=0.6451. It should be noted that the samples from the two animals that had died have atypically higher iron content. This is expected since the death of the animals was from iron overload. In addition, patients with thalassemia most often die as a result of cardiac failure[13], so it is suggested that iron accumulation in the heart also results in death in rats. Figure 3.11 shows the same plot, but with the two animals that died prematurely removed.

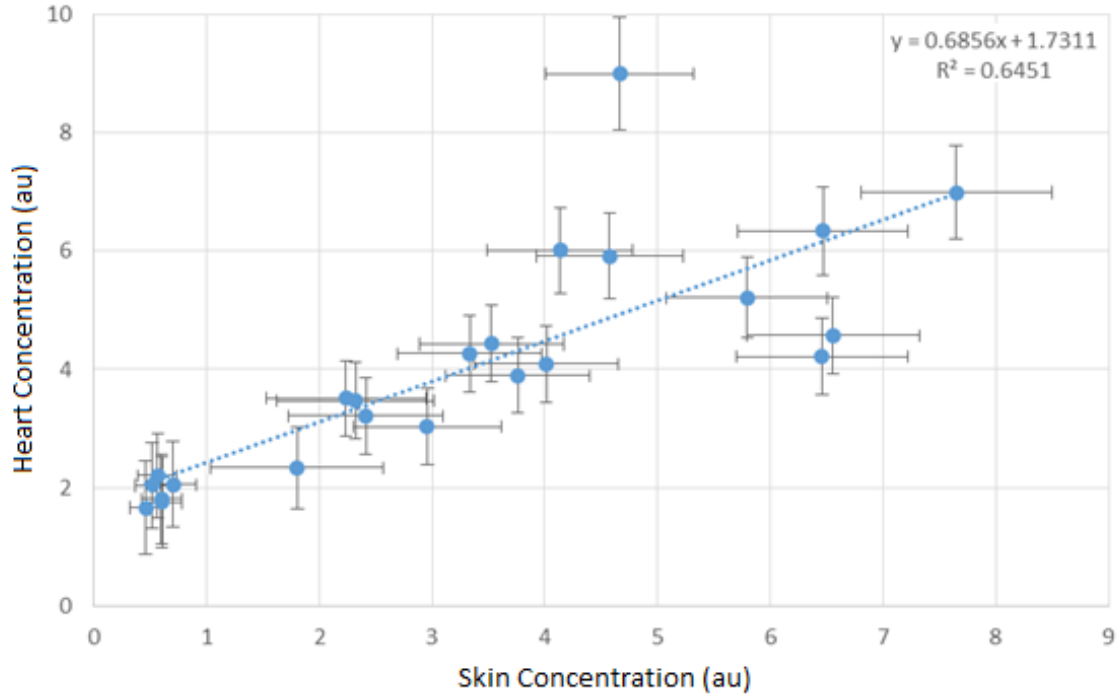

Figure 3.10: Heart iron concentration vs. skin iron concentration, both in arbitrary units, for all animals.

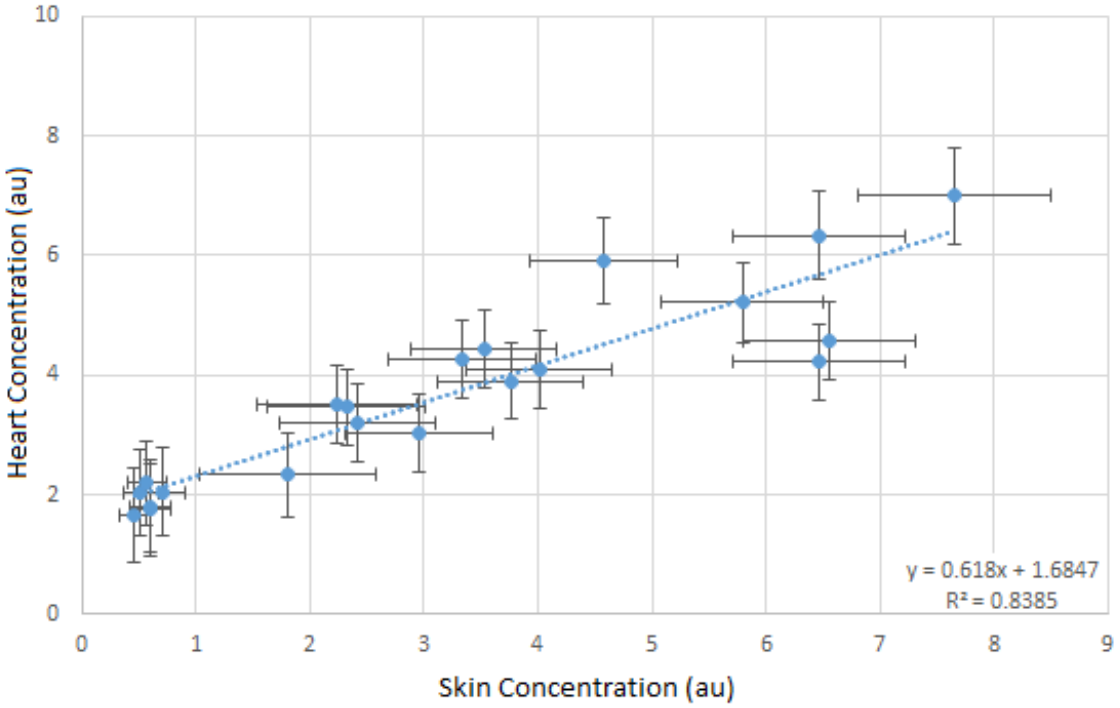

Figure 3.11: Heart iron concentration vs. skin iron concentration, both in arbitrary units, for animals that survived to end of experiment.

It can be seen that the correlation between the skin iron concentration and heart iron concentration is stronger when excluding the animals that died prematurely with R^2=0.84. Similarly, Figures 3.12, 3.13, 3.14, 3.15, 3.16, 3.17 show the correlation between the skin iron concentration and organ iron concentration in all animals and only the animals that survived to end of experiment for the liver, kidney, and spleen, respectively. The liver showed the best fit for a quadratic fit, with R^2=0.89 for n=23 and R^2=0.90 for n=21. The quadratic relationship between liver and skin has been previously mentioned in literature[17]. The kidney and spleen showed the best fit for a linear fit, with R^2=0.78 and R^2=0.69 for n=23, and R^2=0.81 and R^2=0.70 for n=21 for the kidney and spleen respectively.

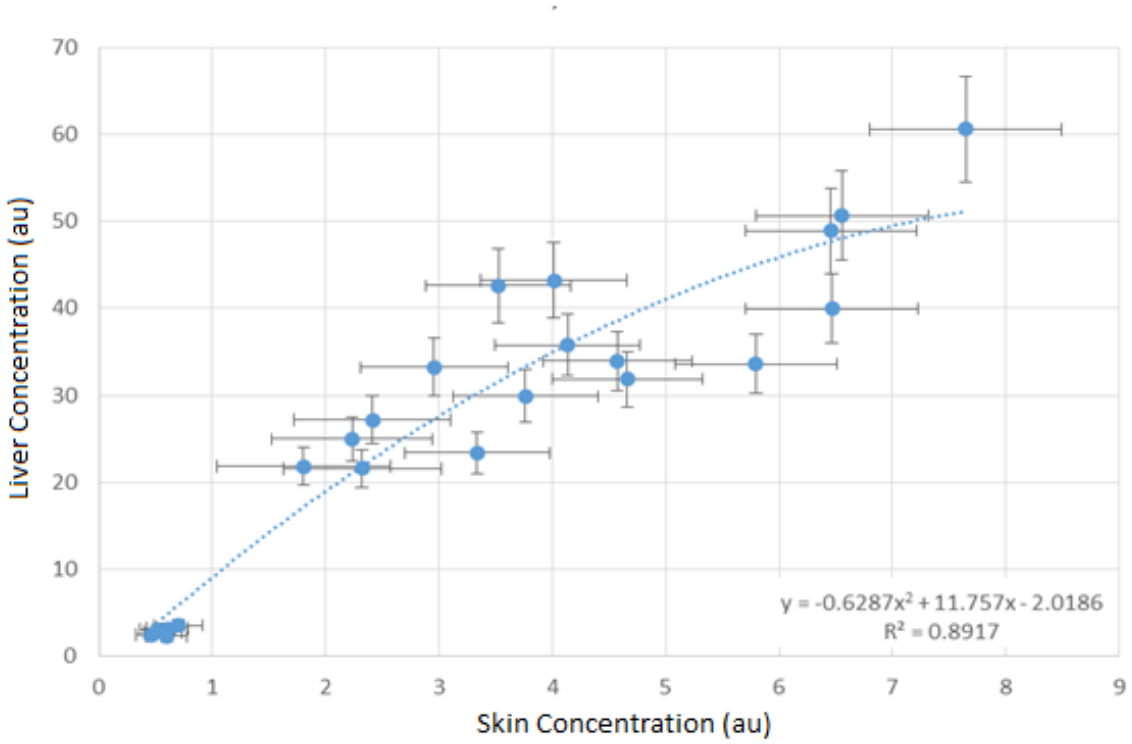

Figure 3.12: Liver iron concentration vs. skin iron concentration for all animals.

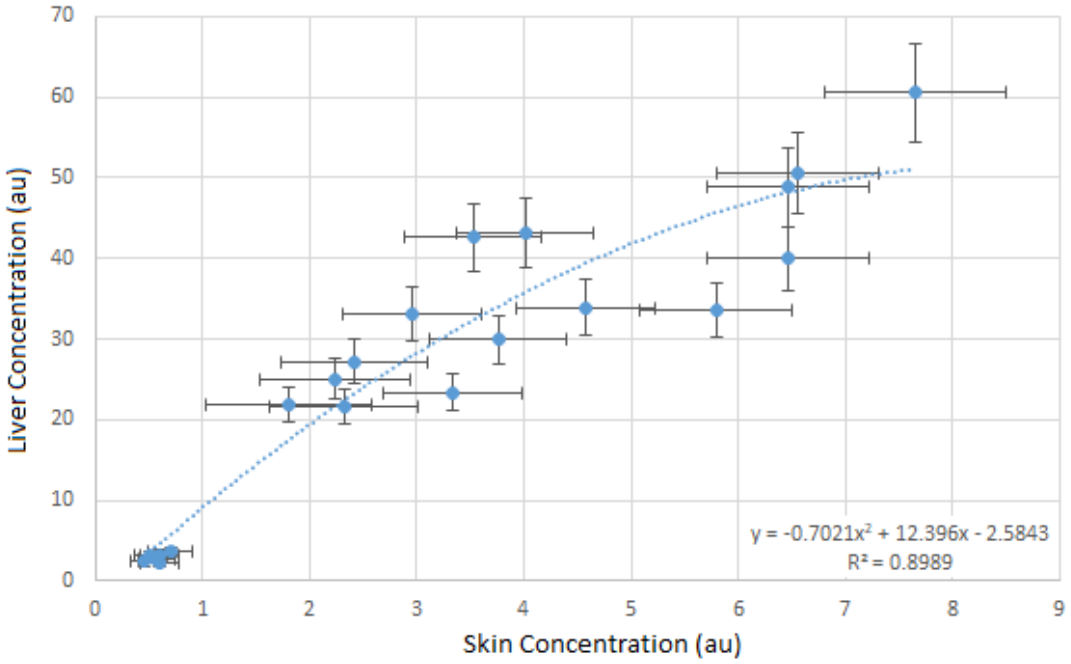

Figure 3.13: Liver iron concentration vs. skin iron concentration for animals that survived to end of experiment.

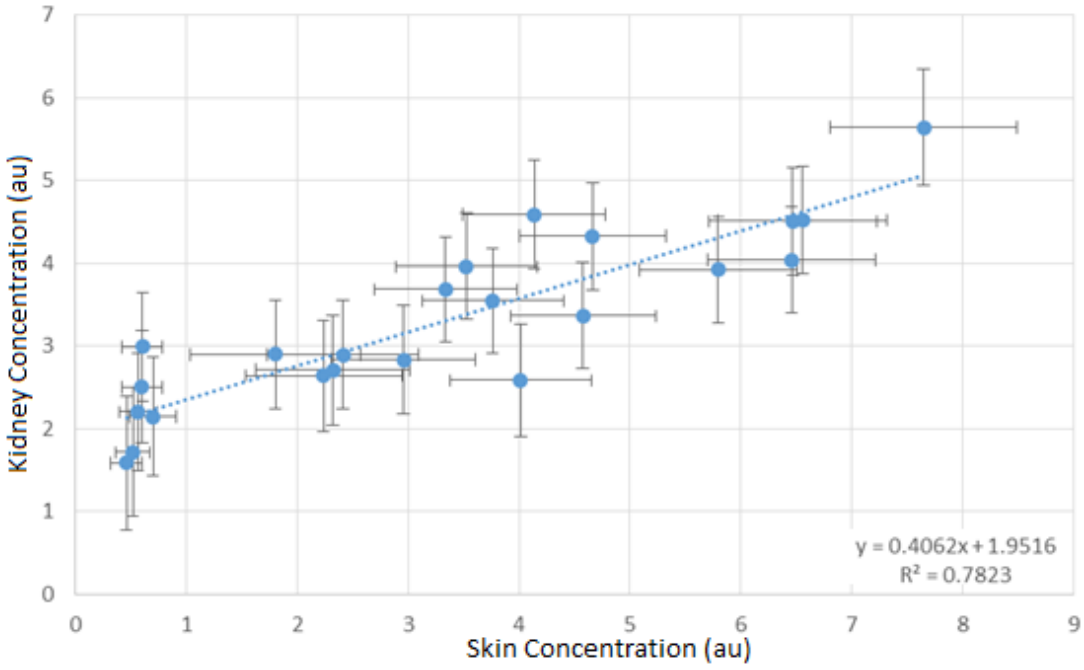

Figure 3.14: Kidney iron concentration vs. skin iron concentration for all animals.

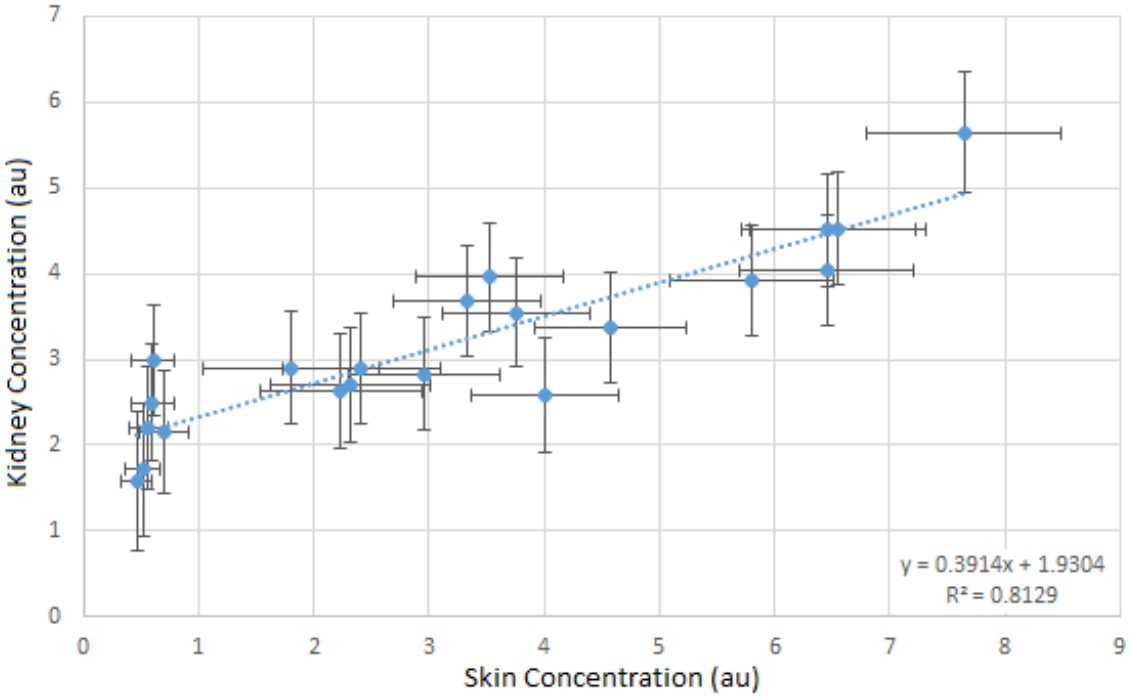

Figure 3.15: Kidney iron concentration vs. skin iron concentration for animals that survived to end of experiment.

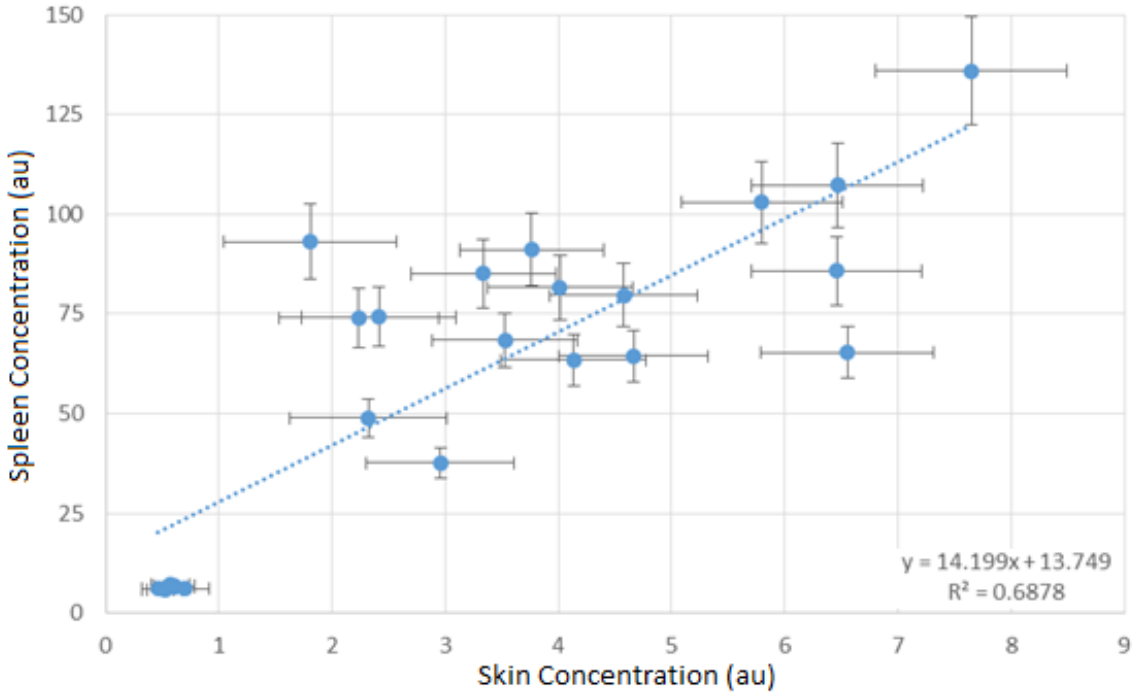

Figure 3.16: Spleen iron concentration vs. skin iron concentration for all animals.

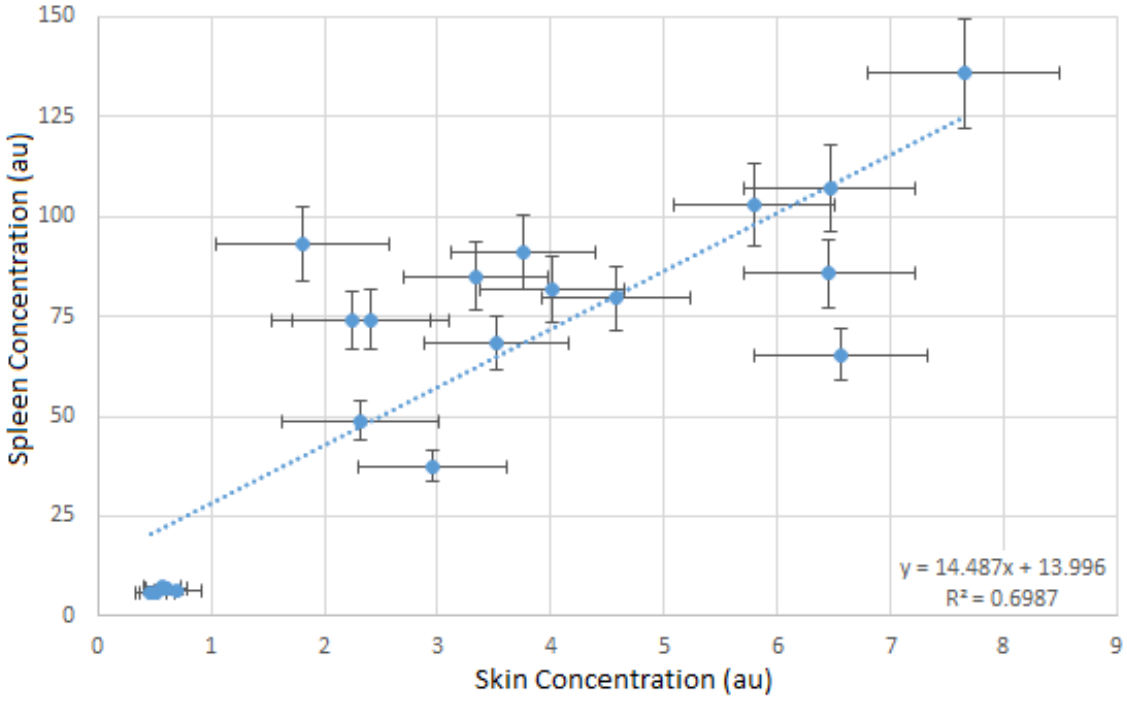

Figure 3.17: Spleen iron concentration vs. skin iron concentration for animals that survived to end of experiment.

The strongest correlation can be seen between the iron concentrations in the skin and liver. The next strongest correlation was observed between the iron in the skin and heart for the animals that survived to the end of the experiment. The greatest disparity between the correlation between all animals and animals that survived to end of experiment was seen for the heart. This suggests that the iron accumulation in the heart is the major cause of death in iron overload.

It is important to note that although the doses administered were either 20mg of Fe^{2+} per week or 40mg of Fe^{2+} per week, the observed accumulation was not as distinct. It appears that the iron distribution in the animals is not consistent between different animals in the same group. Animals that received a larger dose did accumulate more iron, but not at the same rates. As a result, each animal is plotted individually, rather than averaging over a group that received the same dose. This observation also explains why the animals that died were not both from the higher dose group. An animal in Group B had a higher uptake of iron than some of the animals from Group C or D.

3.3.5 Homogeneity

Eight samples were measured at three different locations to investigate homogeneity. The iron concentration for the three locations as well as the mean, standard deviation, and relative standard deviation for each site is shown in Table 3.2.

Table 3.2: The iron concentration, in arbitrary units, for three different locations in a sample as well as the mean, standard deviation, and relative standard deviation for the site.

Site	Location 1	Location 2	Location 3	Mean	Standard Deviation	Relative Standard Deviation (%)
H	4.4	4.9	3.9	4.4	0.5	11.6
K	4.0	3.8	3.0	3.6	0.5	13.8
Lv	43	40	40	41	1	3.1
Sp	68	76	82	76	7	9.2
T	4.0	4.9	4.2	4.4	0.5	10.6
A	3.6	3.3	3.4	3.4	0.2	5.0
LB	3.2	3.1	3.4	3.2	0.2	5.2
UB	3.2	3.5	3.3	3.3	0.1	3.9

The relative standard deviation in the iron concentration for each site ranged between 3.1-13.8%. Considering that the error in the iron concentration of each sample is approximately 10%, from fitting error and counting statistics, this spread in data can be considered reasonable. Therefore, future experiments will not require measurement at multiple sites within the sample holder. One site measurement is sufficient.

3.4 Conclusion

In this experiment, rats were overloaded with iron in two different dose quantities and two injection frequencies to investigate trends in iron accumulation in the heart, liver, kidney, spleen, and skin. It was determined that intraperitoneal injections of 20mg of Fe^{2+}/week and 40mg of Fe^{2+}/week resulted in observable increases in iron in all organs of interest and in the skin. It was also determined that the iron accumulation in an animal was consistent in various skin sites suggesting that future experiments utilizing skin measurements can be done on only one skin site. For all of the skin and organs, it was found that there is no dependency on injection frequency. That is,

an animal receiving a specific dose can have that dose administered in one injection per week, or spread over two injections a week. Lastly, the correlation between organ iron concentration and skin iron concentration was found. A very strong quadratic correlation was found between liver iron concentration and skin iron concentration. A very strong linear correlation was found between heart iron concentration and skin iron concentration, with a dependence on whether the animal survives to end of experiment. Additionally, linear correlations were also observed for skin iron concentration and kidney and spleen iron concentrations. The iron concentration in a sample was found to be homogeneous. Further experiments are warranted to investigate the organ and skin iron concentration relationship with a more varied range of Fe^{2+} doses.

Chapter 4

Iron Overload Study

4.1 Chapter Outline

This chapter presents the results from an experiment in iron overloading rats that have been overloaded in a wide range of iron concentrations. The correlation between skin iron concentration and organ iron concentration was determined using two different XRF systems for the heart, liver, and kidney.

4.2 Materials and Methods

4.2.1 Iron Overloading

In this experiment, eight groups of six male Wistar rats, weighing 126-150g, were intraperitoneally injected with Anem-X iron dextran to deliver doses between 5-40mg Fe^{2+} per week. The same iron dextran solution was administered to all animals, varying only the volume of each injection to deliver different doses. In addition, a group of six Wistar rats were intraperitoneally injected with deionized water once a week to act as the control. All 54 animals in this study were purchased from Charles River Laboratories and housed at the Central Animal Facility at McMaster University. The animals were fed standard rodent chow and drank deionized water *ad libitum*. The experiment was designed so animals received injections for 4 weeks before being given an 8 day equilibration period. The intended doses to be administered is summarized in Table 4.1.

Table 4.1: The intended volumes and the total doses to be administered in this iron overload study.

Group	n	Volume per Dose	Total Volume Administered	Total Dose Administered
Group A	6	0.20mL H_2O	0.8mL	0mg Fe^{2+}
Group B	6	0.05mL Iron Dextran	0.2mL	20mg Fe^{2+}
Group C	6	0.10mL Iron Dextran	0.4mL	40mg Fe^{2+}
Group D	6	0.15mL Iron Dextran	0.6mL	60mg Fe^{2+}
Group E	6	0.20mL Iron Dextran	0.8mL	80mg Fe^{2+}
Group F	6	0.25mL Iron Dextran	1.0mL	100mg Fe^{2+}
Group G	6	0.30mL Iron Dextran	1.2mL	120mg Fe^{2+}
Group H	6	0.35mL Iron Dextran	1.4mL	140mg Fe^{2+}
Group I	6	0.40mL Iron Dextran	1.6mL	160mg Fe^{2+}

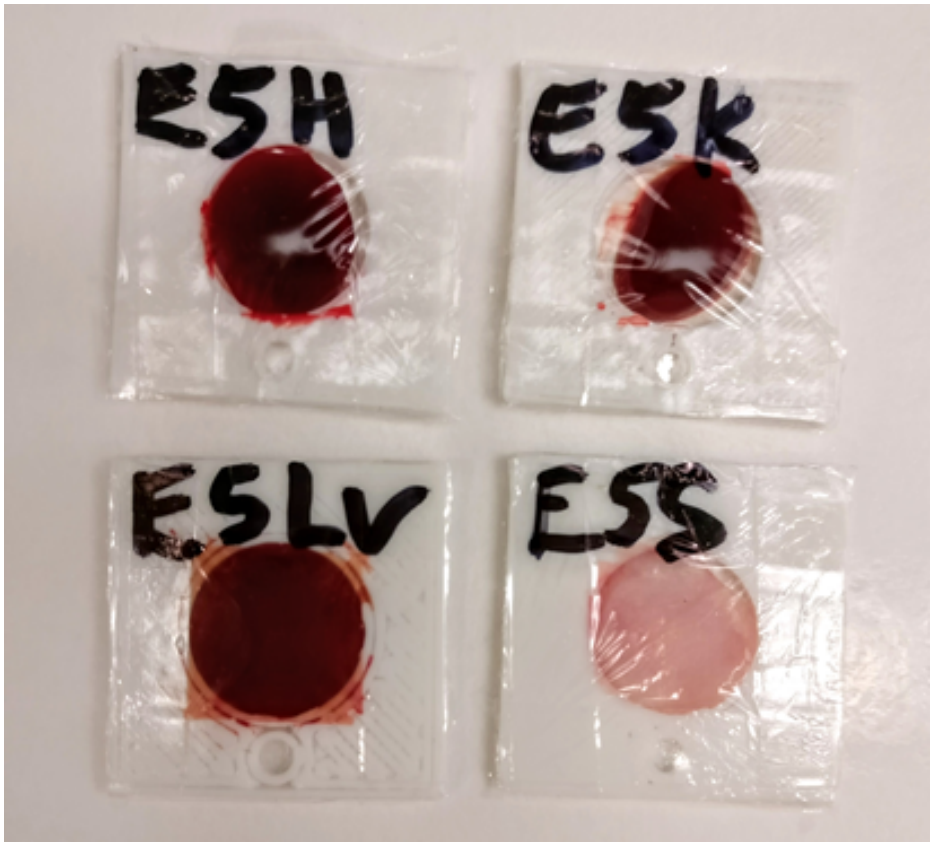

Figure 4.1: Examples of the mounted samples from an animal from Group E.

Following iron overload, organs and skin were collected from the animals in the study. The heart (H), liver (Lv), and kidney (K) were collected since these organs showed the greatest correlation from the results presented in Chapter 3. One 8mm skin (S) biopsy was extracted from each animal in the abdominal area. Only one was collected based on results presented in Chapter 3. Examples of the mounted samples are shown in Figure 4.1.

The same naming convention as the previous studies was used. The name was a string composed of the group the animal was from (A-G), the animal number (between 1-6), and lastly the sample site (H, Lv, K, or S). For example, a skin sample from the control group from the first animal would be called A1S.

4.2.2 XRF Measurements

First, samples were run in the Huber XRF system, using the same procedure and analysis technique as outlined in Section 3.2.2. The samples were again measured for 1 hour at 50mV, 500µA. However, the system was unexpectedly damaged so only 32 samples were measured in the Huber XRF system.

To complete the data set, all the samples were then measured in the Polarized Energy Dispersive X-Ray Fluorescence (PEDXRF) system at McMaster University. The PEDXRF system is a bulk tissue measurement system that requires a very specific geometry, but can significantly reduce scatter from the measured XRF signal. The tungsten anode x-ray tube, at 40kV and 20mA, emits x-rays that pass through two collimators before interacting with a secondary target that is oriented at an angle of 45°. The secondary target used in this experiment was zinc. The Kα characteristic x-rays of the zinc secondary target add 8.64keV x-rays that are close to iron's k-edge, allowing for an increased XRF signal. Following interaction with the secondary target, the x-rays 90° from the primary beam path then pass through an additional two collimators before being incident on the sample, again oriented at an angle of 45°. At this angle, the beam incident on the sample is an ellipse shape, measuring approximately 1cm in diameter in the semi-minor axis, and 1.5cm in the semi-major axis. The XRF signal then passes through two more collimators before being detected with an ORTEC silicon lithium (SiLi) detector. The experiment geometry is shown in Figure 4.2.

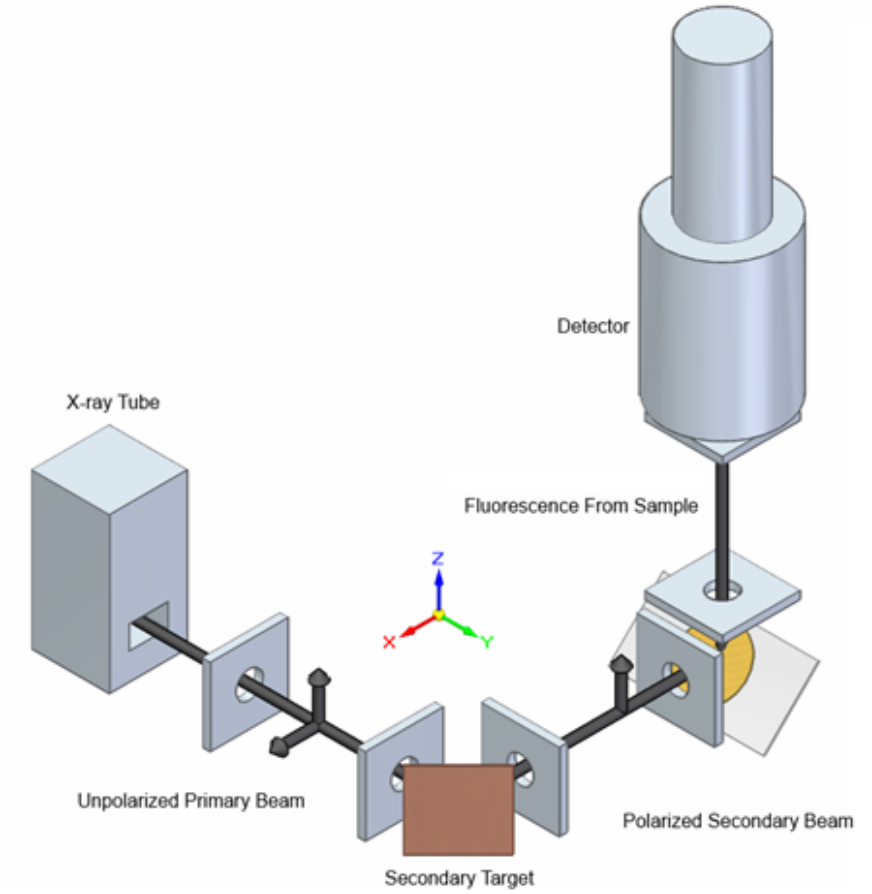

Figure 4.2: The PEDXRF system the samples were measured in[43].

The samples were measured for 30 minutes. The same analysis used in the previous experiments, as outlined in Section 3.2.2, was utilized in this experiment.

4.3 Results & Discussion

4.3.1 General Results

Seven animals died before the end of the experiment. The animals that died were mostly in the higher dose groups, but a few were in the lower dose groups: 1 from Group B, 2 from Group C, 3 from Group G, and 1 from Group H. Since there is no mechanism to remove this excess iron, it was concluded that the longer the animals stayed alive, the greater their risk of dying before the end of experiment. Therefore, the experiment was ended after 3 weeks. The actual doses administered are reported

in Table 4.2. One of the animals from Group G was sent for pathology, but samples were collected for all other animals.

Table 4.2: The actual volumes and the total doses administered in this iron overload study.

Group	n	Volume per Dose	Total Volume Administered	Total Dose Administered
Group A	6	0.20mL H_2O	0.60mL	0mg Fe^{2+}
Group B	6	0.05mL Iron Dextran	0.15mL	15mg Fe^{2+}
Group C	6	0.10mL Iron Dextran	0.30mL	30mg Fe^{2+}
Group D	6	0.15mL Iron Dextran	0.45mL	45mg Fe^{2+}
Group E	6	0.20mL Iron Dextran	0.60mL	60mg Fe^{2+}
Group F	6	0.25mL Iron Dextran	0.75mL	75mg Fe^{2+}
Group G	5	0.30mL Iron Dextran	0.90mL	90mg Fe^{2+}
Group H	6	0.35mL Iron Dextran	1.05mL	105mg Fe^{2+}
Group I	6	0.40mL Iron Dextran	1.20mL	120mg Fe^{2+}

4.3.2 Correlation between Organs and Skin - Huber System

Figures 4.3, 4.4, and 4.5 show the organ iron concentration plotted with skin iron concentration, in arbitrary units, for the heart, liver, and kidney, respectively, as measured in the Huber XRF system. These plots show the data for 32 animals. The 32 animals were the first three animals from each of the nine groups, as well as the fourth animal from Groups A, B, C, H, and I. So, even though this is considered an incomplete data set, it is still evenly distributed between the various groups and can still be representative of trends in the data. Again, the uncertainties in the values are the result of summing the counting error and fitting error in quadrature. Both the heart and kidney show moderately strong linear correlations between organ and skin iron concentrations, with R^2=0.53 and R^2=0.65, respectively. A very strong quadratic correlation between the liver and skin iron concentration was found with R^2=0.92. The measurements on the Huber XRF system show promising results for strong correlations between organ iron concentration and skin iron concentration.

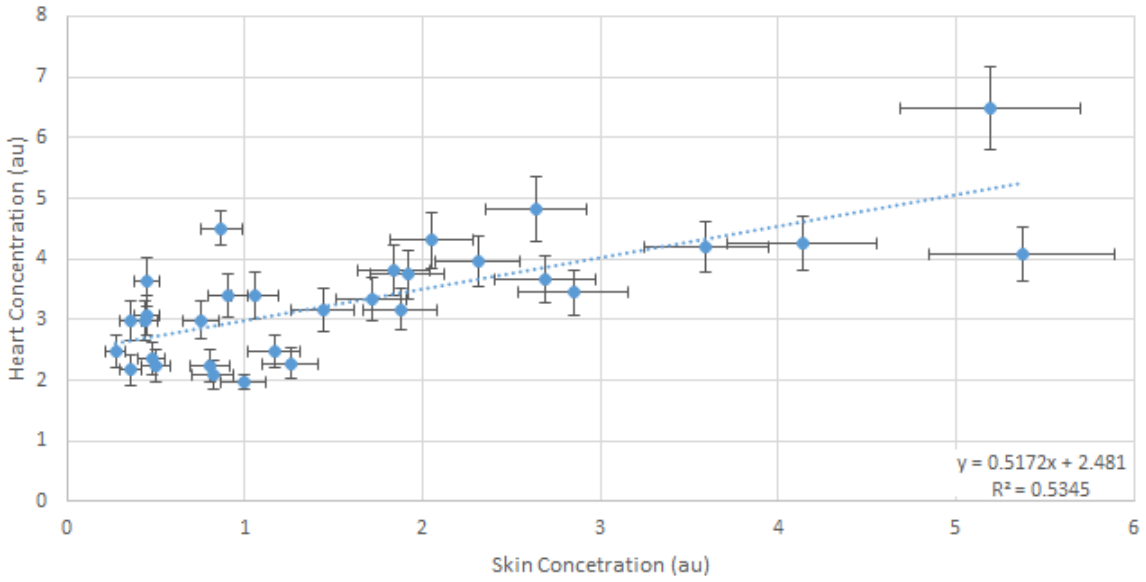

Figure 4.3: Heart iron concentration vs. skin iron concentration, both in arbitrary units, as measured in the Huber XRF system.

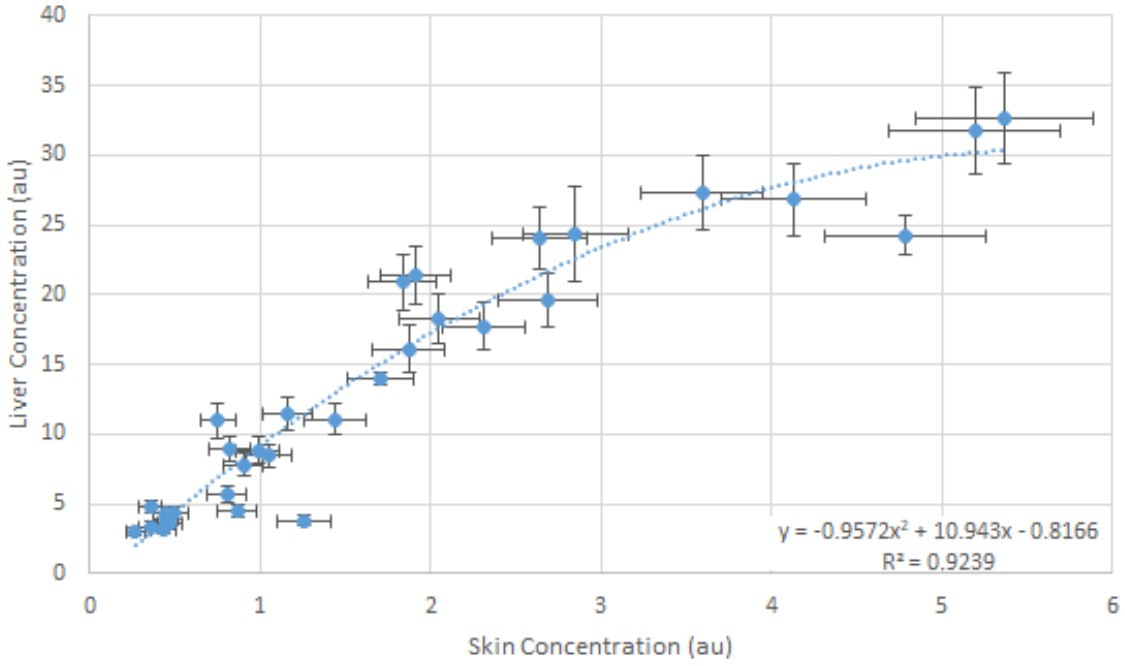

Figure 4.4: Liver iron concentration vs. skin iron concentration, both in arbitrary units, as measured in the Huber XRF system.

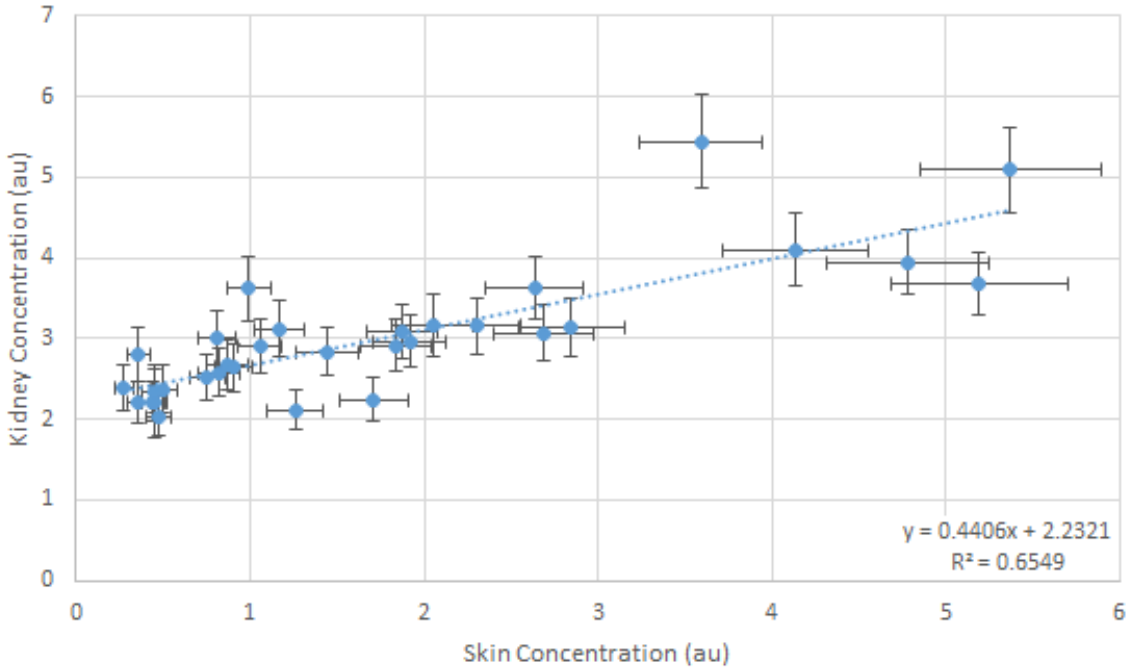

Figure 4.5: Kidney iron concentration vs. skin iron concentration, both in arbitrary units, as measured in the Huber XRF system.

4.3.3 Correlation between Organs and Skin - PEDXRF

Figures 4.6, 4.7, and 4.8, show the organ iron concentration and skin iron concentration for the heart, liver, and kidney for all samples from 53 animals. It can be seen that the data sets contain outliers, defined as points that are less than the first quartile or above the third quartile by more than 1.5 times the interquartile range, and strikes, defined as points that are less than the first quartile or above the third quartile by more than 3 times the interquartile range. With these few outliers and strikes, a weak correlation was found for the heart iron and skin iron concentrations, with R^2=0.1706. There was a moderate correlation for the liver and skin, with R^2=0.578, and there was no correlation found for the kidney and skin, with R^2=0.0028. Outliers and strikes were removed from the data, and the results without these values are plotted in Figures 4.9, 4.10, and 4.11. Note that the PEDXRF system has been calibrated with an iron solution and therefore the concentrations are reported in parts per million (ppm).

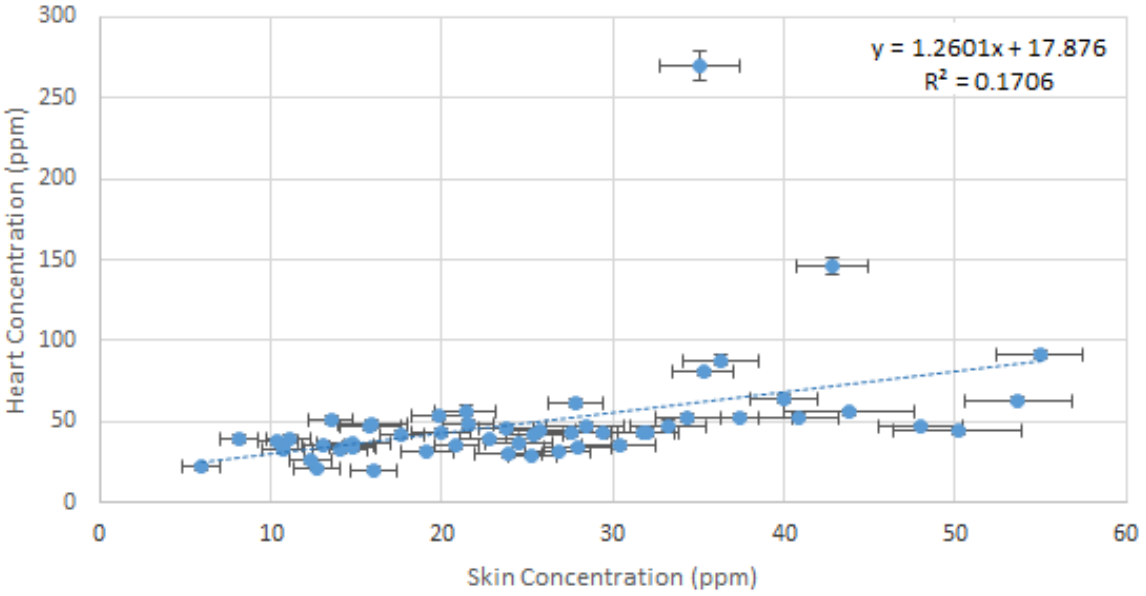

Figure 4.6: Heart iron concentration vs. skin iron concentration, both in parts per million, as measured in the PEDXRF system.

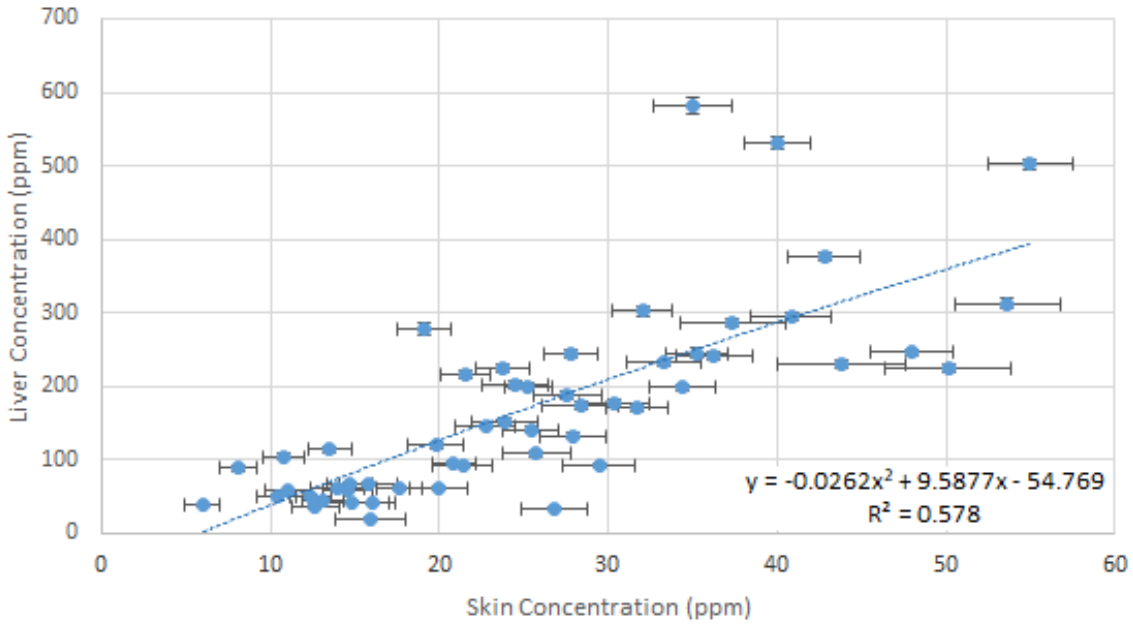

Figure 4.7: Liver iron concentration vs. skin iron concentration, both in parts per million, as measured in the PEDXRF system.

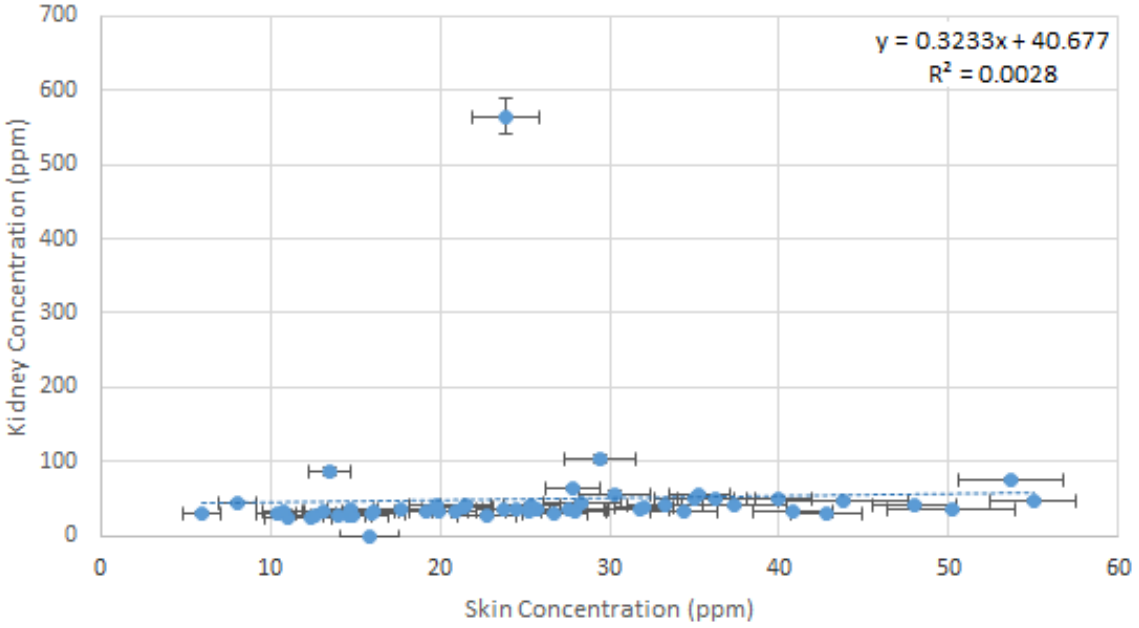

Figure 4.8: Kidney iron concentration vs. skin iron concentration, both in parts per million, as measured in the PEDXRF system.

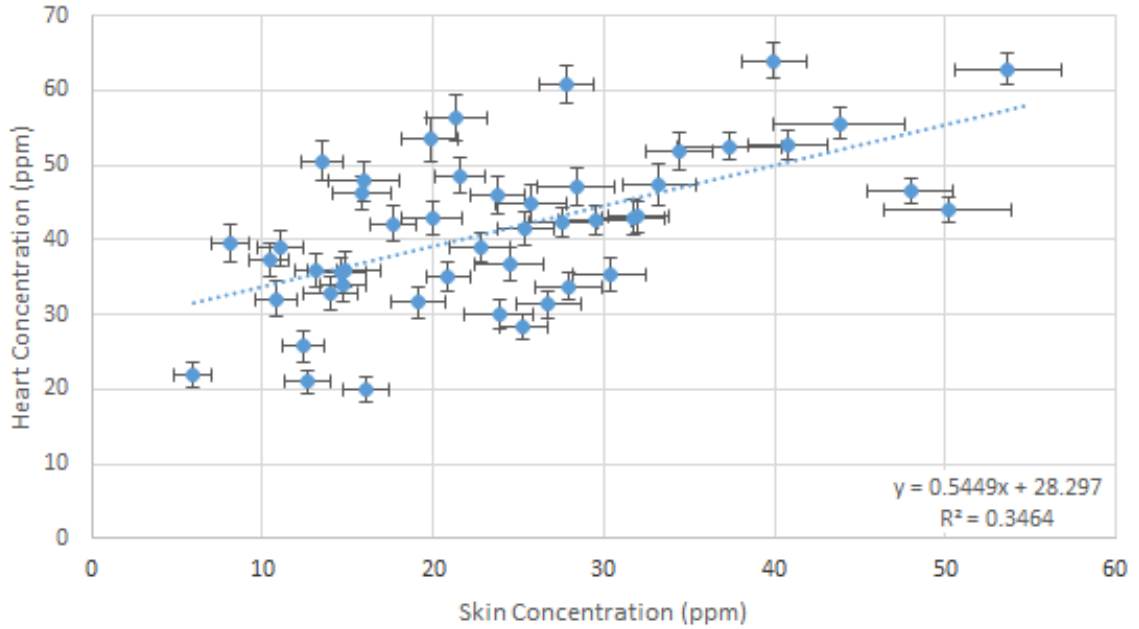

Figure 4.9: Heart iron concentration vs. skin iron concentration, both in parts per million, as measured in the PEDXRF system without strikes or outliers.

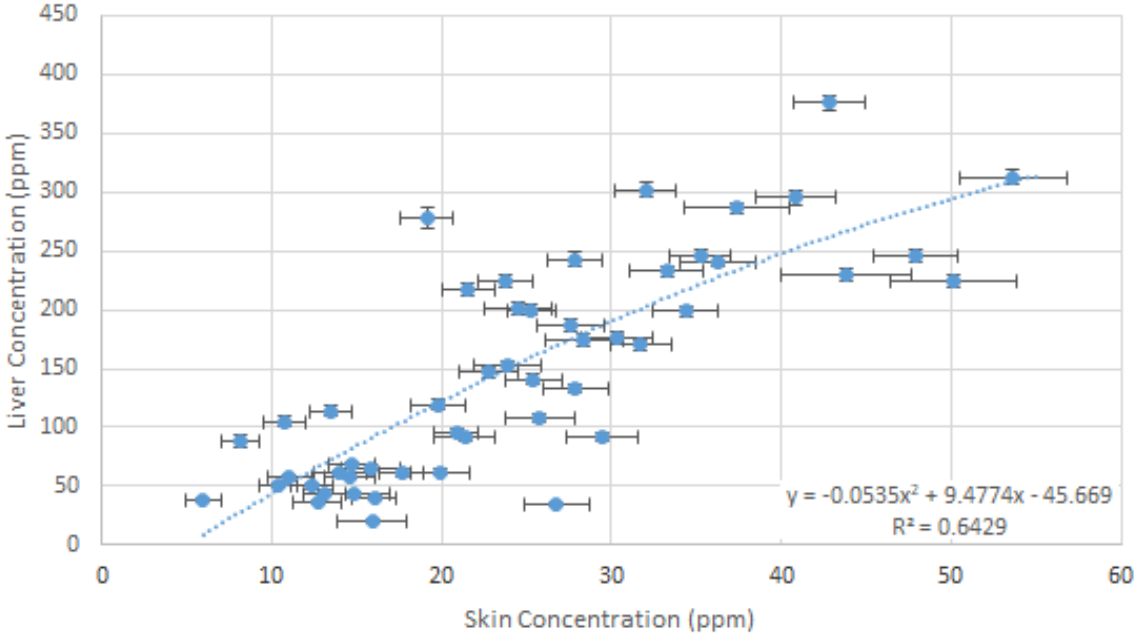

Figure 4.10: Liver iron concentration vs. skin iron concentration, both in parts per million, as measured in the PEDXRF system without outliers.

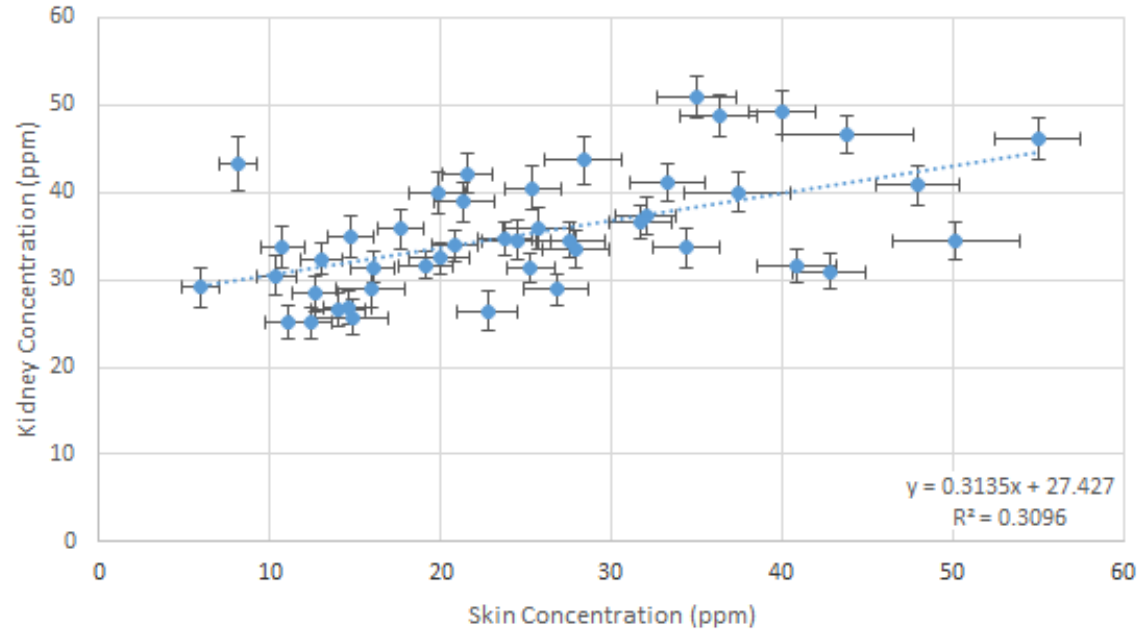

Figure 4.11: Kidney iron concentration vs. skin iron concentration, both in parts per million, as measured in the PEDXRF system without strikes or outliers.

With the outliers and strikes removed, the correlations between organ and skin iron concentrations became stronger. The correlations between organ and skin iron concentration for the heart, liver, and kidney were R^2=0.34, R^2=0.64, and R^2=0.31, respectively. This means that the heart and kidney showed mild correlations, and the liver showed a moderately strong correlation.

Measurements on the PEDXRF system showed weaker correlations compared to the measurements from the Huber XRF system. It was first hypothesized that the differences in correlations were a result in differences in the beam size. The beam size for the Huber system was much smaller than that of the PEDXRF system, approximately 5 times smaller in diameter. It was proposed that a larger beam size might be more heavily influence by hotspots in iron concentrations. However, this is not likely since in the previous chapter, it was determined that the samples were fairly homogeneous. Alternatively, a larger beam size might mean that the beam is incident on an area that is larger than the sample volume. It is suggested that the beam may be measuring the sample as well as some of the sample frame beyond the sample boundary.

In addition, it is believed that the differences in the weaker correlation can be a result of the difference in detector used in the two different systems. Specifically, the PEDXRF detector contains a much smaller active area, meaning that the detector response was not as accurate or precise. The PEDXRF data contained outliers and strikes whereas the Huber system data contained no outliers or strikes.

4.4 Conclusion

In this experiment, rats were overloaded using an iron dextran solution, receiving weekly doses of 5-40mg Fe^{2+}. The correlations between organ iron concentration and skin iron concentration were investigated for the heart, liver, and kidney. When measured in the Huber XRF system, it was found that the the heart and kidney had moderately strong linear correlations with skin, with R^2=0.53 and R^2=0.65, respectively. The liver had a very strong quadratic correlation with skin iron, with R^2=0.92. When measured in the PEDXRF system, weaker correlations were found for all organs. The heart and kidney had a mild correlation with skin iron, with R^2=0.34 and R^2=0.31, respectively. The liver showed a moderately strong correlation with skin iron, with R^2=0.64. It is believed that the differences in the data is a result of the detectors

used in each system. Particularly, the detector used in the PEDXRF system had a smaller active area, resulting in a data set with a greater number of outliers and strikes. This experiment concludes that correlations between organ iron and skin iron concentrations can be observed for the heart, liver, and kidney using two different XRF systems. The liver showed the greatest correlation with skin in both systems, and proves to be the most promising organ of interest for clinical applications. It can then be concluded that skin can best act as a surrogate marker for iron in the liver.

Chapter 5

Portable XRF Measurements

5.1 Chapter Outline

This chapter proposes a device for *in vivo* iron analysis of the skin. The optimal settings for the device are determined. Iron in skin measurements are performed using the samples from Chapter 4. The correlation between skin iron concentration as measured on the portable x-ray fluorescence (PXRF) device and organ iron concentration as measured on the Huber XRF system is reported. Lastly, the device was used to measure skin iron in cadavers to determine the feasibility of measuring *in vivo*.

5.2 Materials and Methods

5.2.1 Portable XRF Device

The Olympus Innov-X Delta Professional Handheld XRF Analyzer is a commercial device commonly used for the elemental analysis of metal alloys or mineral analysis of soil samples. This portable x-ray fluorescence (PXRF) handheld device contains an x-ray excitation source, filters, and a silicon drift detector. The PXRF deviced used in this study contains a gold (Au) source and can operate at 15kV or 40kV.

Figure 5.1: The Olympus Delta Handheld XRF Analyzer.

The software on the PXRF device has an internal camera that has a red ellipse to show the approximate beam size and location. To determine the true beam size, the PXRF device was turned on for five minutes to irradiate radiochromic film. The radiochromic film would then darken to show which area had been irradiated.

5.2.2 Optimal Settings

The PXRF device contains four modes: Soil, Soil-Ca, Alloy Precious, and Mining Plus. The Alloy Precious and Mining Plus modes offer real-time analysis of samples, and the internal software reports concentration data. These two modes do not offer the option to export the raw spectrum for separate analysis. As such, the two Soil modes were selected as the modes of operation to allow for independent analysis. Both the Soil and Soil-Ca modes have the same beam output, but the internal algorithm for analysis varies. Since independent analysis will be performed, either mode can be used. The Soil mode will be selected for consistency.

The Soil mode has three x-ray beams that can be used. Beams 1 and 2 utilize a 40kV tube, while Beam 3 utilizes a 15kV tube. Beams 1 and 2 run with a 100.551mA current, and Beam 3 runs with a 200.662mA current. In addition, each beam has its own unique filtration. The exact details of which materials and what thicknesses are used as filters is proprietary, and this information was not disclosed to the user. To determine which beam should be used, two iron skin phantoms made of epoxy resin were obtained in concentrations of 12ppm and 225ppm. The 12ppm sample is considered the low concentration sample, and this concentration is approximately the same order of magnitude expected in human skin. The 225ppm is a higher concentration used to amplify any trends that might exist in the data.

To determine which counting time is ideal, a rat skin sample from the control group (A4S) in Chapter 4 was measured for 1, 3, 5, 10 , 15 minute intervals. Then, the relative error in the counts was calculated. This sample was selected to optimize settings for a sample that would have a relatively weak XRF signal.

5.2.3 PXRF Calibration

In order to associate the measured counts to a ppm concentration, a proper iron calibration must be performed. A 1000μg/mL iron (III) nitrate solution was diluted with deionized water to make 0, 2, 4, 6, 8, 10, 15, 20, 35, and 50ppm solutions. The

same sample holders utilized in Chapter 4 were filled with each of the solutions and were measured in the PXRF for 10 minutes. The spectra collected were analyzed in the PeakFit software to find the integral area under each iron peak to create a calibration curve.

5.2.4 PXRF Correlation

The 32 samples measured in the Huber XRF system in Chapter 4 were also measured in the PXRF system to investigate possible correlations between skin iron measurements made on the PXRF with organ iron concentration measurements made on the Huber XRF system. To simulate an *in vivo* environment, tissue phantoms were designed, modelled, and fabricated using 3D plastic printing technology. An "infinitely thick" tissue backing was created using polylactic acid (PLA) plastic. The sample is inserted into a slot within a 5cm thick block to simulate x-ray scatter from tissue. This tissue backing is shown in Figure 5.2. To simulate the scatter that would result from tissue and bone, a tissue and bone backing was created using the same PLA. The sample would insert into a slit that is on top of 1mm thick PLA. On the other side of the PLA a 1mm thick aluminum square was inserted to imitate bone. This tissue and bone backing is shown in Figure 5.3.

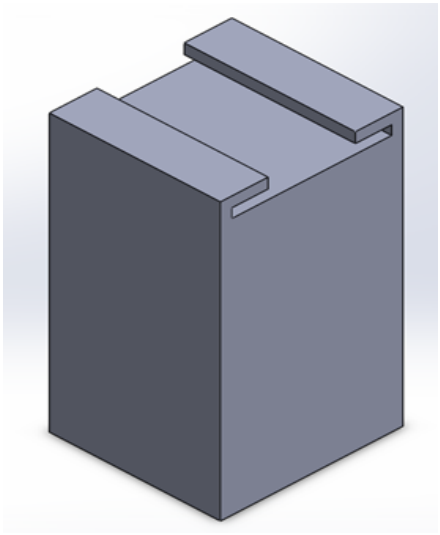

Figure 5.2: The "infinitely thick" tissue.

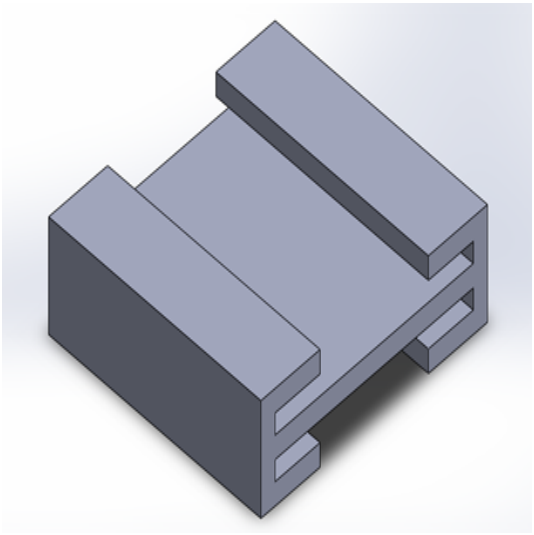

Figure 5.3: The tissue and bone backing.

The PXRF device was mounted in its benchtop system, locked into a stainless steel box. In this setup, the handheld allows for hands free measurement. The handheld is connected to a computer with the Olympus Innov-X software that allows for real time

data display and collection. Each skin sample was placed in the tissue backing and on the PXRF device. Using the internal camera on the device, the beam was centered on the sample. Figure 5.5 shows a captured image of a rat skin sample placed in the "infinitely thick" blue plastic backing. The red ellipse shows the approximate location of the beam.

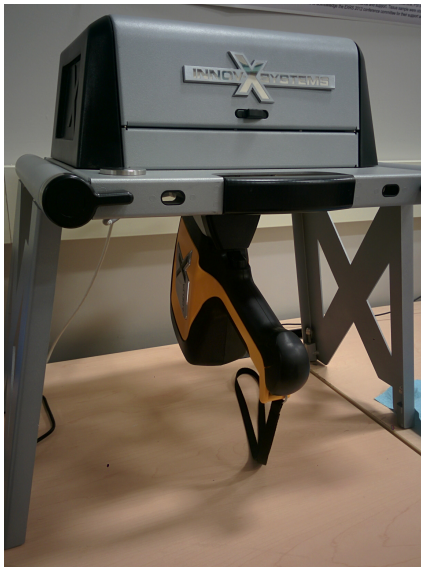

Figure 5.4: The PXRF device mounted in the benchtop system.

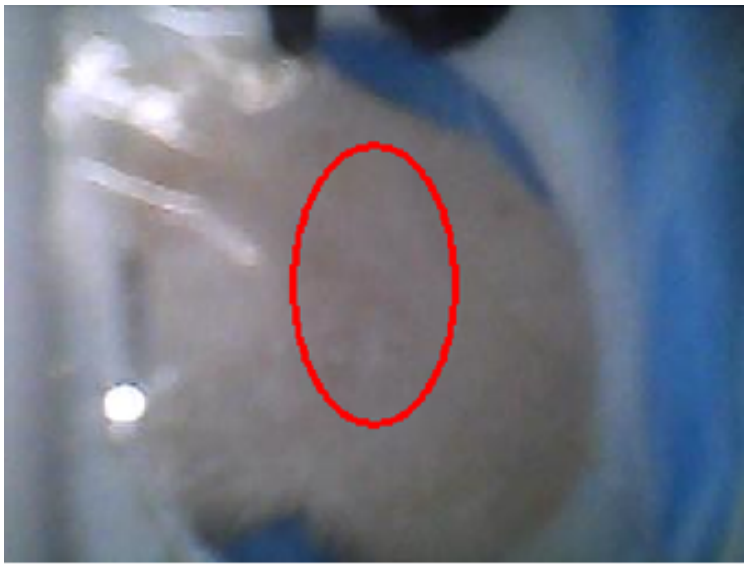

Figure 5.5: The skin from a rat sample (I4S) before measurement in the PXRF system. The beam position is outlined in the red ellipse.

5.2.5 Cadaver Measurements

Four cadavers were measured using the PXRF device at 13 various sites throughout the body. The PXRF was operated using the 15kV (Beam 3) tube in the Soil mode. The sites included the thenar eminence, between metacarpophalangeal joints 1 & 2, between metacarpophalangeal joints 2 & 3, at the lateral malleolus, plantar arch, surprasternal notch, xiphoid process, at the middle of the patella, above the acromioclavicular joint, at the coracoid process of the scapula, popliteal fossa, olecranon process, and in the middle of the gluteus maximus. These sites were selected to span most of the body. The sites chosen were mostly near bony landmarks to enable the greatest reproducibility. The measured signal for each of the sites was compared to investigate possible differences in iron accumulation in different sites.

5.3 Results & Discussion

5.3.1 Determination of True Beam Size

Figure 5.6 shows the radiochromic film prior to and following a 5 minute exposure with 15kV (Beam 3) in the Soil mode. It can be seen that the radiochromic film has darkened where the true beam was penetrating the film. Despite the beam indicator showing a 5mm beam, the true beam is 8mm in diameter. Figure 5.7 shows the size of the true beam.

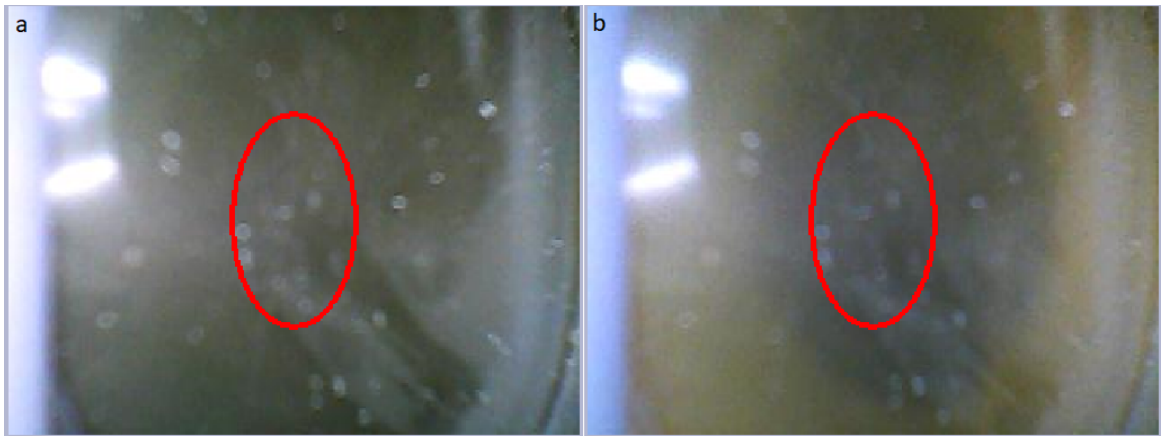

Figure 5.6: a) The radiochromic film prior to irradiation. The red ellipse is the beam size indicator on the device software. b) The radiochromic film following a 5 minute irradiation. A dark circle larger than the red ellipse can be seen. This is the true beam size.

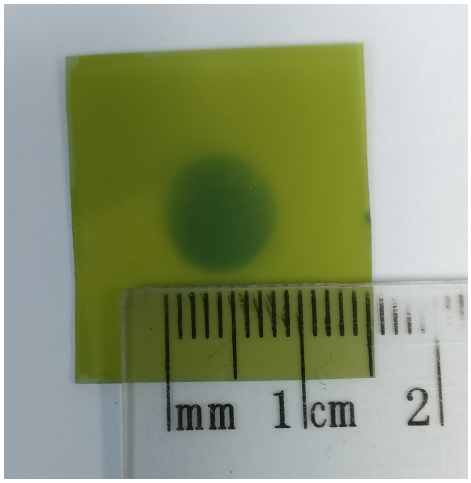

Figure 5.7: The true beam size of the PXRF device with a diameter of 8mm.

5.3.2 Optimal Settings

Iron skin phantoms made from epoxy resin were measured with each of the three beams in the Soil mode. Figure 5.8 shows the measured spectrum for a 12ppm iron skin phantom measured with each of the three beams in the Soil mode.

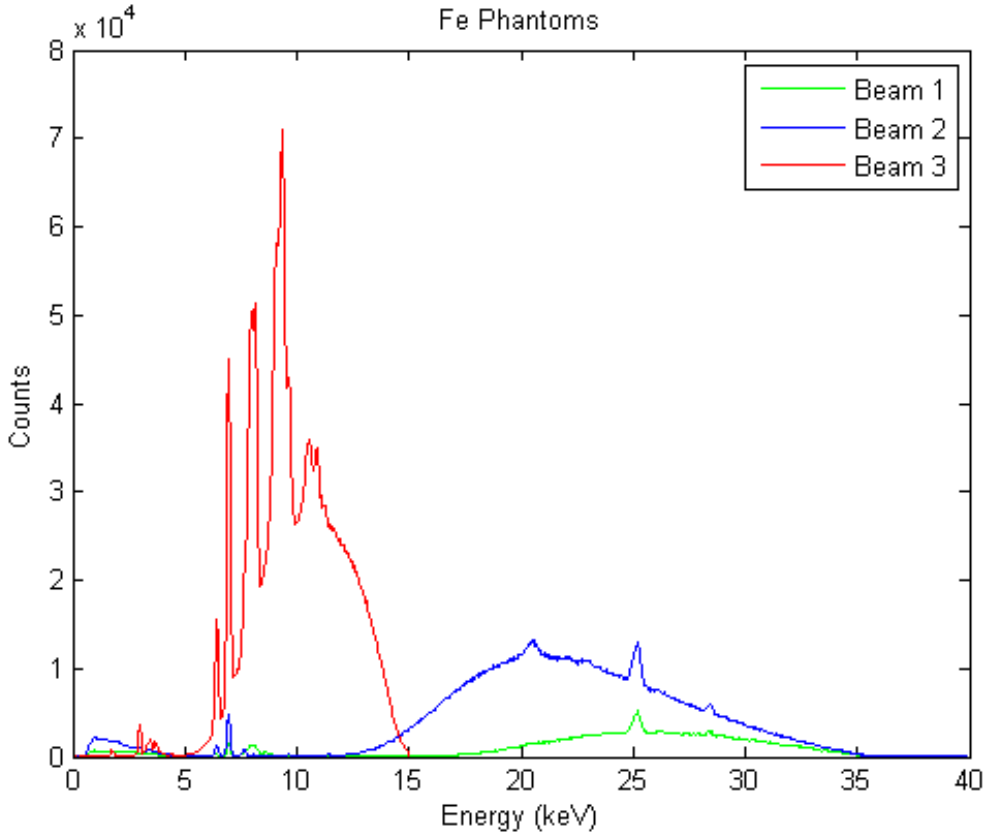

Figure 5.8: The spectrum for a 12ppm iron skin phantom measured with each of the three beams in the Soil mode.

To determine which beam would be best for measuring iron, the 12ppm and 225ppm iron skin phantoms were measured with each of the beams. The counts were normalized to the maximum count to account for the different current settings of each beam. Figures 5.9 and 5.10 plot the resulting spectra for the 12ppm and 225ppm iron phantom, respectively.

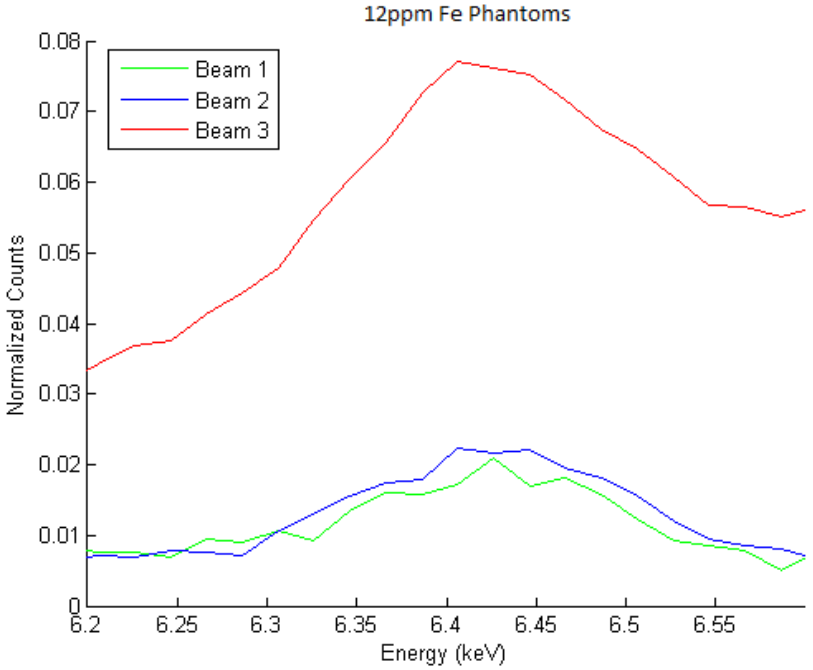

Figure 5.9: The spectrum for a 12ppm iron skin phantom measured with each beam.

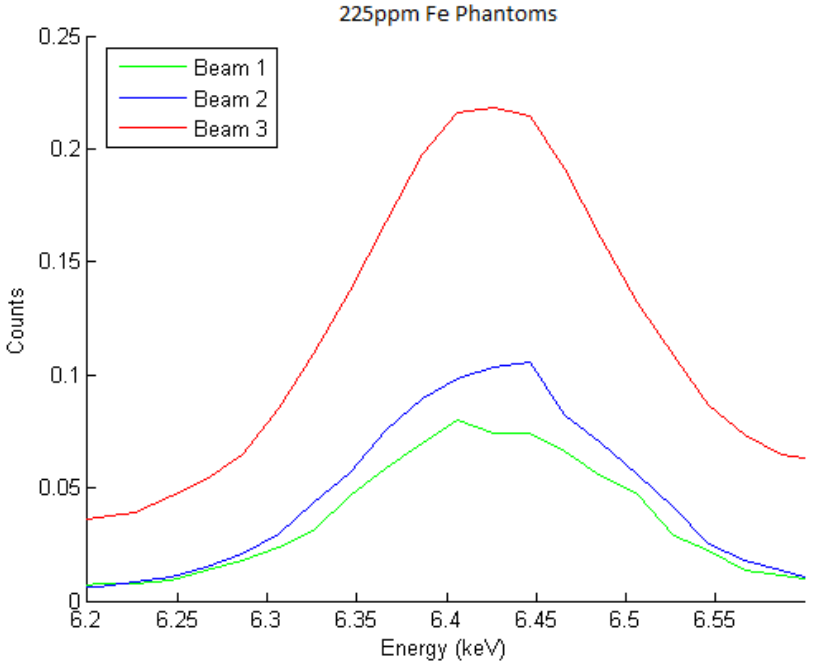

Figure 5.10: The spectrum for a 225ppm iron skin phantom measured with each beam.

It can be seen that the signal from Beam 3 is the greatest for both concentrations. For a quantitative comparison, the signal-to-noise ratio (SNR) was calculated for the iron peaks of each beam. Assuming a linear background, the SNR is the ratio between the peak height, and the square root of the average of the height of the background on either side of the peak. From Figure 5.9, the SNR is given by:

$$SNR_{Beam1} = \frac{Counts(6.4keV)}{\sqrt{\frac{Counts(6.25keV)+Counts(6.55keV)}{2}}} \tag{5.1}$$

$$= \frac{94}{\sqrt{\frac{38+47}{2}}} \tag{5.2}$$

$$= 14.42 \tag{5.3}$$

Simiarly, the SNR for Beam 2 is 28.82 and the SNR for Beam 3 is 99.37. Therefore, it can be concluded that Beam 3 is the optimal setting for the detection of iron using the PXRF system.

5.3.3 PXRF Calibration

Figure 5.11 shows the calibration curve obtained from measuring the iron calibration samples as measured in the PXRF device. The iron counts were normalized to argon.

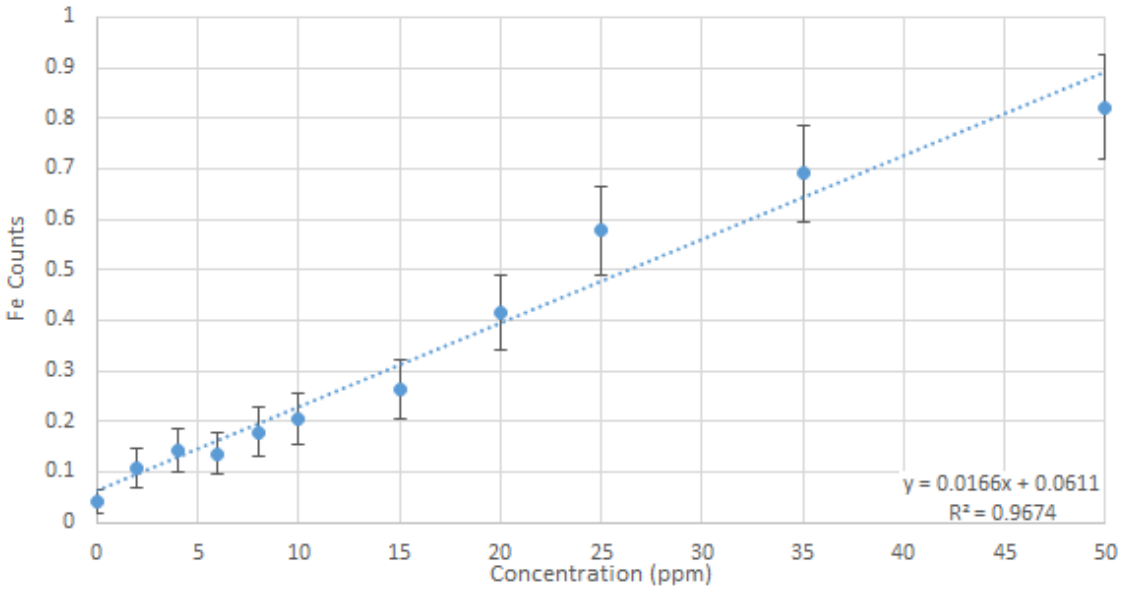

Figure 5.11: The iron calibration curve for the PXRF system.

The iron solutions made strongly followed a linear trend. Therefore, future studies using the PXRF device to measure iron can utilize the following equation to convert the peak area, in counts and normalized to argon, to a ppm concentration:

$$Concentration[ppm] = \frac{Counts - 0.0611}{0.0166} \tag{5.4}$$

5.3.4 PXRF Correlation

Figures 5.12, 5.13, and 5.14 display the organ iron concentration for the heart, liver, and kidney, respectively, as measured on the Huber XRF system, and the skin iron concentration as measured in the PXRF system. The heart showed a moderate correlation with the skin with R^2=0.45. The liver showed the best correlation, with a moderately strong correlation with R^2=0.74. The kidney showed the weakest correlation, with a mild correlation with R^2=0.36. From these results, it can be concluded that the liver shows the best correlation with skin iron as measured on the PXRF device.

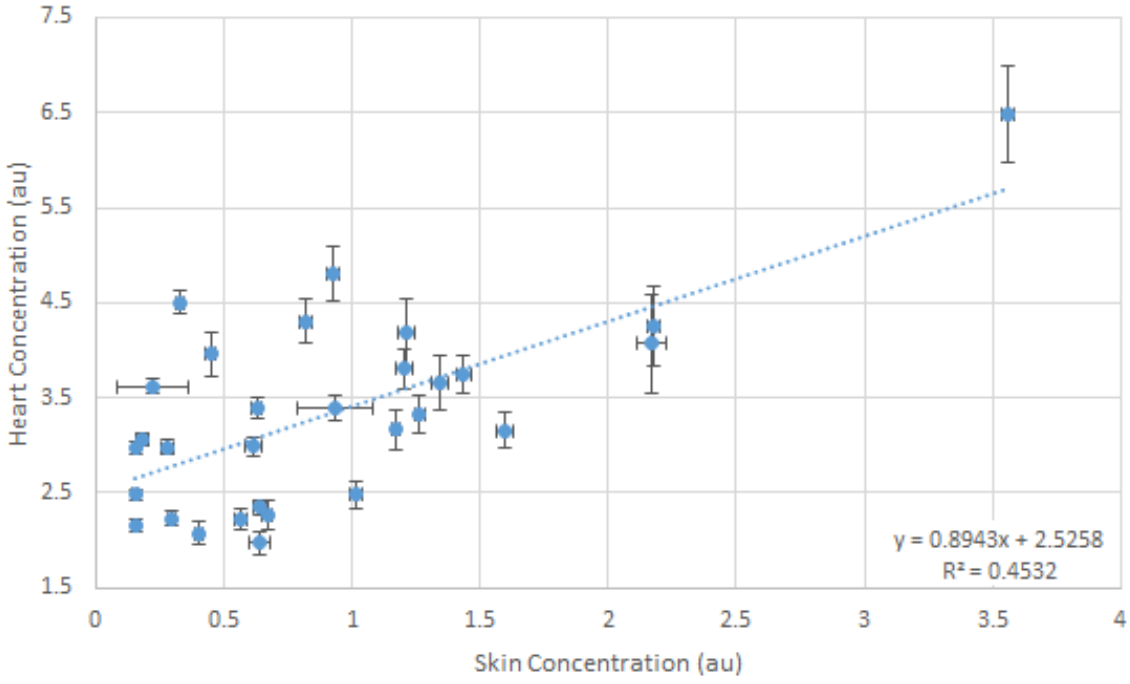

Figure 5.12: Heart iron concentration, as measured in the Huber XRF system, vs. skin iron concentration, both in arbitrary units, as measured in the PXRF system.

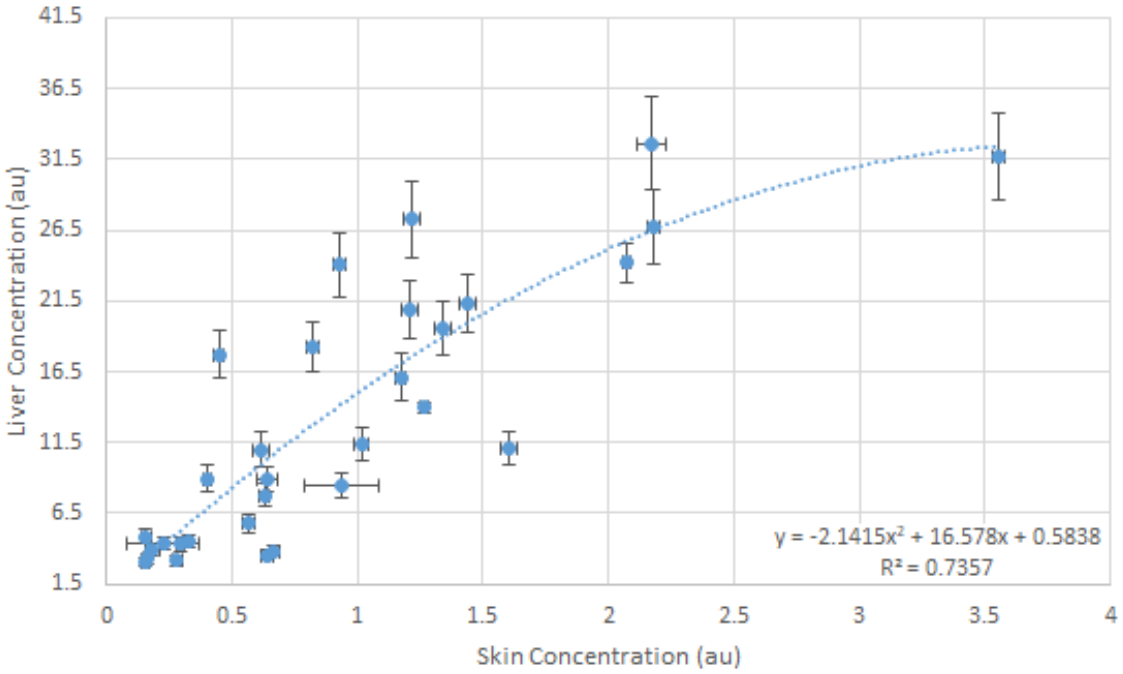

Figure 5.13: Liver iron concentration, as measured in the Huber XRF system, vs. skin iron concentration, both in arbitrary units, as measured in the PXRF system.

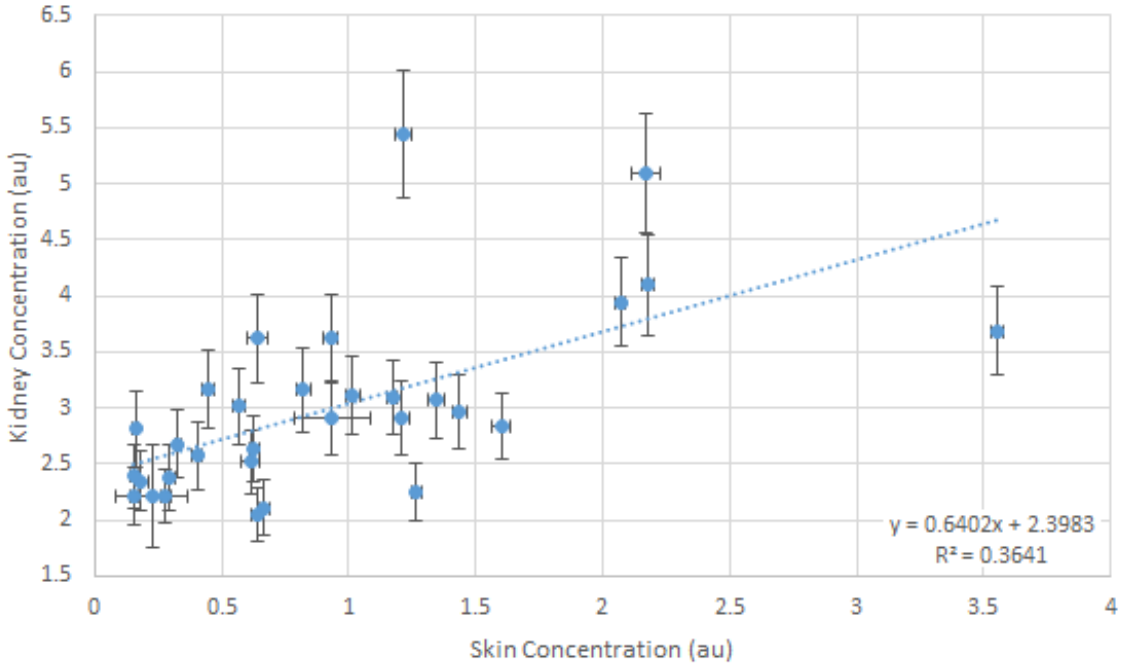

Figure 5.14: Kidney iron concentration, as measured in the Huber XRF system, vs. skin iron concentration, both in arbitrary units, as measured in the PXRF system.

The iron concentration measured in the skin ranged from 0.15-3.56 arbitrary units. Using Equation 5.4 to convert to ppm, this means that the concentration of iron in rat skin ranged from 5.36-211ppm. It should be noted that since a correction factor for epidermal thickness was not applied, the true iron concentration would be higher than this range due to self absorption.

It has been demonstrated that the PXRF device shows promise as a tool for iron analysis in rats. The device is able to measure very low concentrations of iron. It is seen that the skin iron concentration measured using the PXRF correlates with organ iron concentration, with a moderately strong correlation between the liver and skin.

5.3.5 Cadaver Measurements

The skin of cadavers were measured using the PXRF device. Sites of interest include: the thenar eminence (TE), between metacarpophalangeal joints 1 & 2 (MJ12), between metacarpophalangeal joints 2 & 3 (MJ23), at the lateral malleolus (LM), plantar arch (PA), surprasternal notch (SN), xiphoid process (XP), at the middle of the patella (P), above the acromioclavicular joint (AJ), at the coracoid process of the scapula (S), popliteal fossa (PF), olecranon process (O), and in the middle of the gluteus maximus (GM). Resolvable peaks were measured for all samples. Figure 5.15 shows sample spectra from each of the sites from cadaver 13.

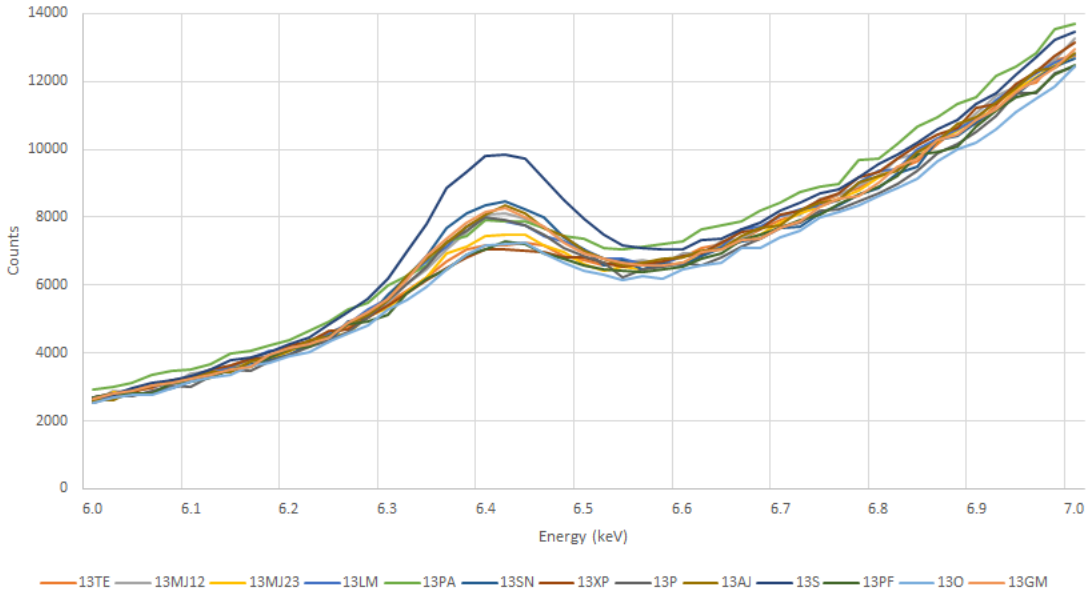

Figure 5.15: Raw XRF spectra for 13 skin sites for cadaver 13.

Iron peaks for almost all of the sites are almost identical. The only site that was slightly higher for cadaver 13 was at the lateral malleolus. This cadaver had visible reddening in the ankle area. When a person dies, the orientation of the body may result in blood pooling in a particular area, also known as livor mortis. As a result, the iron concentration in that area of the body may be higher. This effect is more clearly seen in Figure 5.16 which shows the spectra for 12 skin sites on cadaver 11.

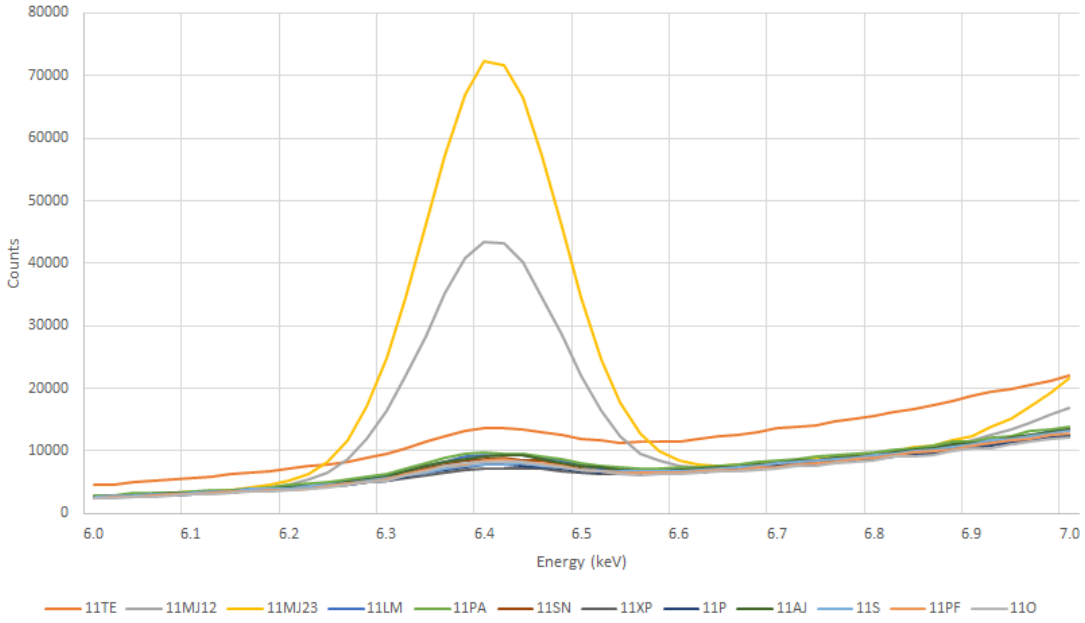

Figure 5.16: Raw XRF spectra for 12 skin sites for cadaver 11.

This person appears to have died with one arm lower than the rest of the body, with the palm of the hand facing up. This cadaver had red areas around the hands, particularly on the back of the hand. In Figure 5.16, the two sites that had the highest iron peaks were between metacarpophalangeal joints 1 & 2 (MJ12) and between metacarpophalangeal joints 2 & 3 (MJ23). Both of these sites were on the back of the hand. The thenar eminence (TE) was slightly higher, but not to the extent of MJ12 or MJ23. Other areas where reddening was commonly observed were the acromioclavicular joint (AJ) and at the coracoid process of the scapula (S). It is believed this is due to most patients dying in a supine position. Despite this effect, most of the sites do produce similar, or even identical, XRF responses. Therefore, it has been concluded that the number of sites to be measured in future studies can be reduced.

It is suggested that four sites be measured in future cadaver measurements: thenar eminence (TE), metacarphalangeal joints 1 & 2 (MJ12), at the peak of the patella (P), and at the plantar arch (PA). These sites are varied enough that it is unlikely that all of these sites will have blood pooling. In addition, since these sites are located at extremities, the radiation dose delivered will be less significant than for doses delivered to the torso or near critical organs.

5.3.6 Conclusion

The PXRF device was investigated and found to be useful for skin iron measurements. First, the beam size was determined using radiochromic film. The beam was 8mm in diameter as opposed to the 5mm indicated by the manufacturer. It was found that Beam 3 in the Soil mode was the best setting for measuring iron since it resulted in the greatest signal-to-noise ratio of 99.37. The PXRF was calibrated using iron (III) nitrate solutions and a calibration curve was determined in order to convert from counts to ppm concentrations. This conversion is stated in Equation 5.4. The correlation between skin iron concentrations as measured on the PXRF device and organ iron concentrations as measured on the Huber XRF system was found for the heart, liver, and kidney. The kidney showed the weakest correlation; there was a slight correlation with the skin, with R^2=0.36. The heart showed a moderate correlation with the skin, with R^2=0.45. The liver showed the best correlation, with a moderately strong correlation with R^2=0.74. It is then concluded that the PXRF device can be used as a tool for measuring iron in skin to act as a surrogate marker for organ iron concentration at the very least in rats. Lastly, the PXRF device was used to measure skin iron in human cadavers. Resolvable iron peaks were found for all skin sites measured. Skin sites typically contained the same iron content; however, body orientation at time of death results in blood pooling which disrupts skin iron measurements. As a result, four skin sites from the extremities were selected as sites of interest in future studies to avoid blood pooling due to people dying and remaining in a supine position. These sites also reduce the impact of the radiation dose associated with the XRF device. The PXRF device is a promising tool for *in vivo* skin iron measurement.

Chapter 6

Dosimetry

6.1 Chapter Outline

This chapter presents dosimetry measurements for the PXRF device. Multiple experiments were conducted to estimate the dose from an irradiation using this device. The feasibility of using this device to measure humans will be discussed.

6.2 Materials & Methods

6.2.1 Electronic Radiation Dosimeter

A DMC-3000 electronic radiation dosimeter purchased from Mirion Technologies was used to provide an estimate of the radiation dose from an Olympus Innov-X Delta Professional Handheld XRF analyzer. This device has a small screen that reports the cumulative dose in real time in units of mrem (1mrem=0.01mSv). The device was irradiated for 1 minute, 3 minutes, 5 minutes, and 8 minutes. All measurements utilized Beam 3 (15kV) in the Soil mode.

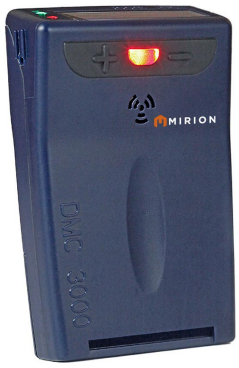

Figure 6.1: The DMC-3000 electronic radiation dosimeter.

6.2.2 Lithium Fluoride Thermoluminescent Dosimeters

Nine lithium fluoride (LiF) thermoluminescent dosimeters (TLDs) purchased from Mirion Technologies were irradiated using the same PXRF device. These TLD chips were translucent and colourless 3mm×3mm squares that give tissue equivalent dose. Each chip was aligned with the beam indicator on the PXRF device with the "infinitely thick" tissue backing, as shown in Figure 6.3. Three chips were irradiated for 3 minutes, three chips were irradiated for 5 minutes, and three chips were irradiated for 10 minutes. All measurements utilized Beam 3 (15kV) in the Soil mode. These chips were then sent back to Mirion Technologies to be read and dose quantities were provided.

Figure 6.2: The TLDs utilized in this experiment.

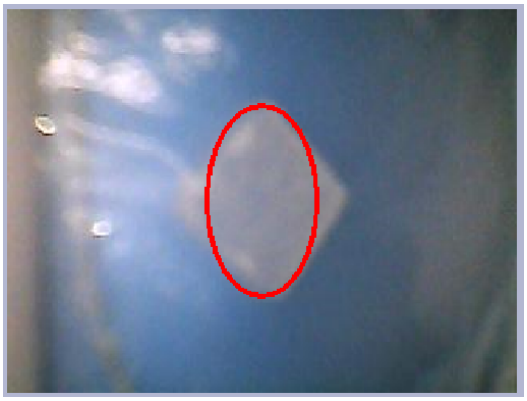

Figure 6.3: The TLD as shown in the internal camera of the PXRF device.

6.2.3 Optically Stimulated Luminescence Dosimeters

Five nanoDot™ optically stimulated luminescence dosimeters (OSLDs), purchased from Landauer Inc., were irradiated using the same PXRF device. These 1cm×1cm dosimeters are skin equivalent, meaning the dosimeters behave under radiation stress in a similar manner to skin. Each OSLD was aligned using the internal camera of the PXRF device and the tissue backing was placed on top, as seen in Figure 6.5. Two of the OSLDs were irradiated for 5 minutes, and three were irradiated for 10 minutes. All measurements utilized Beam 3 (15kV) in the Soil mode. These chips were given to the McMaster Health Physics department to be read and absorbed dose quantities were provided.

Figure 6.4: A nanoDot™ OSLD.

Figure 6.5: A nanoDot™ OSLD aligned in the internal camera of the PXRF device.

6.3 Results & Discussion

6.3.1 Electronic Radiation Dosimeter

The DMC-3000 reports effective dose, and the results from this experiment are summarized in Table 6.1.

Table 6.1: The measured effective doses from the DMC-3000.

Trial	Time (min)	Start (mrem)	End (mrem)	Total Dose (mrem)	Total Dose (μSv)
1	1	8.2	8.7	0.5	5
2	3	8.7	10.6	1.9	19
3	5	10.6	13.7	3.1	31
4	8	13.7	18.4	4.7	47

It is estimated that the effective dose from the PXRF device as measured on the electronic radiation dosimeter is between 5-6μSv/min. A shortcoming of this device is that the dosimeter chip is under a hard plastic case. It is then assumed that this dose estimate is an underestimate since this plastic will attenuate a portion of the beam before reaching the dosimeter chip below. The following experiment utilizes a dosimeter chip that is not enclosed in plastic.

6.3.2 Lithium Fluoride Thermoluminescent Dosimeters

The total effective doses as measured by the LiF TLDs are summarized in Table 6.2.

Table 6.2: The total measured effective doses from the LiF TLDs.

Chip	Time (min)	Total Effective Dose (mSv)
1	3	0.22
2	3	0.24
3	3	0.24
4	5	0.22
5	5	0.78
6	5	0.19
7	10	2.95
8	10	0.21
9	10	0.26

The doses reported by Mirion for these chips were very unexpected. With two exceptions, most of the doses for all of the chips were approximately 0.24mSv, regardless of irradiation time. It was discovered that the LiF TLDs used in this experiment are only calibrated for energies greater than 15keV. Therefore, since almost all of the x-ray output is lower than 15keV, these LiF TLDs are not a reliable method of calculating radiation dose. The next experiment utilizes a dosimeter with a more useful energy range.

6.3.3 Optically Stimulated Luminescence Dosimeters

The OSLDs used in this experiment have a useful energy range of 5keV to 20MeV and are skin equivalent. These chips are accurate within 10% in this energy range. The OSLDs also have the capability of being read multiple times. Table 6.3 summarizes the measured absorbed dose, average equivalent dose rate, and average effective dose rate for each of the OSLDs used in this experiment.

Table 6.3: The average equivalent and effective doses and standard deviation as measured with the OSLDs. The errors on absorbed dose values are ±10%.

Chip	Time (min)	Absorbed Dose (Gy)	Average Equivalent Dose Rate (mSv/min)	Average Effective Dose Rate (mSv/min)
1	5	1.2 1.1 1.2 1.0 1.1	220±20	2.2±0.2
2	5	1.2 1.2 1.2 1.2 1.1	221±6	2.2±0.06
3	10	2.3 2.2 2.2 2.1 2.2	240±10	2.4±0.1
4	10	2.5 2.4 2.5 2.5 2.2	250±10	2.5±0.1
5	10	2.7 2.3 2.5 2.5 2.6	240±10	2.4±0.1

The average equivalent and effective dose rates received by the OSLDs were 230±10mSv/min and 2.3±0.1mSv/min, respectively. Previous studies using PXRF devices have attempted dosimetry to assess radiation risk. A 2017 study proposing the use of an Olympus Innov-X Delta XRF analyzer, the same device used in this study, reports the equivalent dose to be 15±4mSv and approximately $8\times10^{-3}\mu$Sv for 120s exposure times[44]. This estimate is multiple orders of magnitude lower than the doses measured in this study. There are a few key differences between the previous

study and this study. Firstly, the published study used Beam 2, whereas this study utilized Beam 3. The 40kV x-ray tube of Beam 2 would result in a slightly lower skin dose than the 15kV x-ray tube of Beam 3; however, the x-rays would still deposit in tissue so the effective dose should be similar. In addition, the study utilized LiF TLDs, which as previously discussed, is not an appropriate measurement device for the PXRF system since it is only calibrated to 15keV x-rays. Even for a 40kV x-ray spectrum, a significant portion of the beam is not accurately being measured. Also, these lower energy x-rays would be the greatest contributors to radiation dose. It is believed that since the OSLDs are calibrated to a lower energy, the doses measured in this experiment, although higher, are more accurate.

The effective dose rate from this machine poses very little radiation risk. A five minute exposure to the beam would result in the same amount of dose as a computed tomography of the abdomen or pelvis, approximately 10mSv[45]. However, when analysing risk for a skin exposure, it is much more meaningful to look at the absorbed dose, or equivalent dose. Since skin is a very large organ and has such a low tissue weighting factor, doses that are averaged over the entire body become very small values. Irradiances that are concentrated in a small area may result in immediate effects such as erythema or dermal necrosis without increasing the risk of skin cancer by a significant amount.

It has been reported that potential effects of early transient erythema, a slight reddening of the skin, can occur from a single exposure of 2Gy and main erythema can occur from a single exposure of 6Gy[46]. This means that a 10 minute exposure to this device could potentially cause biological damage in the skin. It appears that the feasibility of using this device in a clinical setting is significantly dependent on counting time and the settings used for measurements. Future experiments are planned to measured the absorbed dose from much shorter measurement times, one minute or less, and for different settings.

6.4 Conclusion

In conclusion, dosimetry was performed on the Olympus Innov-X Delta Professional Handheld XRF analyzer using three different dosimetry devices. The most accurate dosimetry was measured using optically stimulated luminescence dosimeters (OSLDs) which are calibrated for energies between 5keV-20MeV. When the system is in the

Soil mode using only Beam 3, it was found that the equivalent and effective dose rates were 230±10mSv/min and 2.3±0.1mSv/min, respectively. Although this dose would result in a very low effective dose, it results in a significant equivalent dose. Therefore, the use of this device in a clinical setting is highly dependent on the measurement time and the settings used. Future experiments are planned to outline the optimal procedure for use in a clinical application.

Chapter 7

Conclusion and Future Work

Five major experiments were conducted to determine the feasibility of using skin XRF measurements as a marker for iron levels in various organs in the body.

Firstly, a comparison in iron overloading techniques was performed. Rats were overloaded with iron through ingestion and intraperitoneal injection. Although both techniques resulted in increases of iron in the heart, liver, and skin, the injection method showed a greater difference. In addition, injection proved to be a more efficient technique, requiring less time for dose administration per animal. Therefore, it was determined that intraperitoneal injection is a much more effective method of iron overloading than ingestion.

Next, a preliminary investigation in the correlation between skin iron concentration and organ iron concentration was performed. Rats were injected once a week with 20mg Fe^{2+}, once a week with 40mg Fe^{2+}, or twice a week with 20mg Fe^{2+}. Heart, liver, kidney, spleen, and four skin samples were collected from each animal and measured in the Huber XRF system. A very strong quadratic correlation was found between liver iron concentration and skin iron concentration, with R^2=0.90. A very strong linear correlation was found between heart iron concentration and skin iron concentration, with R^2=0.84. Similarly, a very strong linear correlation was found between kidney iron concentration and skin iron concentration, with R^2=0.81. A linear correlation was also found between spleen iron concentration and skin iron concentration, with R^2=0.70. There were no observable differences between animals that received the same dose in one or in two injections. Therefore, it can be concluded that there is no dependency on injection frequency. The iron concentration within a sample was found to be homogeneous.

The primary investigation in the correlation between skin iron concentration and organ iron concentration was then conducted. Rats were overloaded with iron in a larger variety of dose increments; animals received weekly doses of between 5-40mg Fe^{2+}. When measured in the Huber XRF system, it was found that the heart and kidney had moderately strong linear correlations with R^2=0.53 and R^2=0.65, respectively. The liver had a very strong quadratic relationship with skin iron, with R^2=0.92. Weaker correlations were found when the samples were measured in the PEDXRF system. The heart and kidney had mild correlations with R^2=0.34 and R^2=0.31, respectively, and the liver had a moderately strong quadratic correlation with R^2=0.64. Since the liver iron levels showed the greatest correlation with skin iron levels in both systems, it proves to be the most promising organ of interest in clinical applications.

The Olympus Innov-X Delta Professional Handheld XRF Analyzer was proposed as a portable XRF measurement device to measure skin iron concentrations *in vivo*. Rat skin samples from the previous experiment were measured using the portable XRF device to compare with organ iron concentrations as measured in the Huber XRF system. The liver showed the best correlation of the organs investigated, with a moderately strong quadratic correlation, with R^2=0.74. The heart showed a moderate linear correlation, with R^2=0.45. The kidney showed the weakest correlation with skin iron concentration, with R^2=0.36. The portable XRF device was also used to measure the skin of human cadavers. All sites measured resulted in detectable levels of iron. It is recommended that future human measurements be made on skin sites of extremities to reduce the effect of blood pooling and to reduce radiation risk. It has been demonstrated that the portable XRF device can be used as a tool for measuring skin iron concentration to act as a surrogate for organ iron concentration. Future work involves investigating the correlation between skin iron concentration and organ iron concentration in humans.

Lastly, multiple dosimetry experiments were carried out to determine the radiation risk associated with an irradiation from the portable XRF device. When measured with optically stimulated luminescence dosimeters (OSLDs), equivalent and effective dose rates were 230±10mSv/min and 2.3±0.1mSv/min, respectively, when the device is operated with Beam 3 of the Soil mode. These quantities indicate low risk of long term health effects, but concerns regarding erythema can be expected. As such, the use of this device in a clinical setting can be considered for short measurement times. More dosimetry measurements with the portable XRF device are warranted to investigate

the radiation risk for the device's various beams and modes.

In conclusion, it has been demonstrated that skin iron concentrations can act as a surrogate marker for organ iron concentration, especially for the liver. In addition, the Olympus Innov-X Delta Professional Handheld XRF Analzyer shows great promise as the measurement tool for *in vivo* skin iron assessment.

Bibliography

[1] N. Andrews, "Disorders of Iron Metabolism," *The New England Journal of Medicine*, vol. 341, pp. 1986–1995, 1999.

[2] F. Jawad, "Iron in the Human Body," *Journal of Pakistan Medical Association*, pp. 332–334, 1996.

[3] L. Gomella and S. Haist, *Clinician's Pocket Reference*. New York: The McGraw-Hill Companies, 2007.

[4] A. Pietrangelo, "Hereditary Hemochromatosis — A New Look at an Old Disease," *Library*, pp. 2383–2397, 2004.

[5] C. H. Society, "Hemochromatosis - How Common is It ? The Most Common Genetic Disorder in the Western World," p. 300, 1996.

[6] C. Niederau, R. Fischer, A. Pürschel, W. Stremmel, D. Häussinger, and G. Strohmeyer, "Long-term survival in patients with hereditary hemochromatosis." *Gastroenterology*, vol. 110, pp. 1107–19, 1996.

[7] A. Tavill, "Diagnosis and Management of Hemochromatosis," *Hepatology*, vol. 33, no. 5, pp. 1321–1328, 2001.

[8] H. Kazazian, "The Thalassemia Syndromes: Molecular Basis and Prenatal Diagnosis in 1990," *Semin Hematol*, vol. 27, no. 3, pp. 209–28, 1990.

[9] E. P. Vichinsky, E. A. Macklin, J. S. Waye, F. Lorey, and N. F. Olivieri, "Changes in the Epidemiology of Thalassemia in North America: A New Minority Disease," *Pediatrics*, vol. 116, no. 6, pp. 818–825, 2005.

[10] G. Whipple and W. Bradford, "Racial or Familial Anemia of Children: Associated with Fundamental Disturbances of Bone and Pigment Metabolism," *American Journal of Diseases of Children*, vol. 42, no. 2, pp. 336–365, 1932.

[11] N. F. Olivieri and G. M. Brittenham, "Iron-Chelating Therapy and the Treatment of Thalassemia," *The Journal of The American Society of Hematology*, vol. 89, no. 3, pp. 739–761, 1997.

[12] A. D. Heys and T. L. Dormandy, "Lipid peroxidation in iron-overloaded spleens," vol. 60, pp. 295–301, 1981.

[13] E. Poggiali, E. Cassinerio, L. Zanaboni, and M. D. Cappellini, "An update on iron chelation therapy," *Blood Transfusion*, vol. 10, no. 4, pp. 411–422, 2012.

[14] C. Borgna-Pignatti, S. Rugolotto, P. De Stefano, H. Zhao, M. D. Cappellini, G. C. Del Vecchio, M. A. Romeo, G. L. Forni, M. R. Gamberini, R. Ghilardi, A. Piga, and A. Cnaan, "Survival and complications in patients with thalassemia major treated with transfusion and deferoxamine," *Haematologica*, vol. 89, no. 10, pp. 1187–1193, 2004.

[15] M. J. Cunningham, E. A. Macklin, E. J. Neufeld, and A. R. Cohen, "Complications of beta-thalassemia major in North America." *Blood*, vol. 104, no. 1, pp. 34–9, 2004.

[16] I. T. Gilmore, A. Burroughs, I. M. Murray-Lyon, R. Williams, D. Jenkins, and A. Hopkins, "Indications, methods, and outcomes of percutaneous liver biopsy in England and Wales: an audit by the British Society of Gastroenterology and the Royal College of Physicians of London." *Gut*, vol. 36, no. 3, pp. 437–41, 1995.

[17] M. J. Farquharson, A. P. Bagshaw, J. B. Porter, and R. D. Abeysinghe, "The use of skin Fe levels as a surrogate marker for organ Fe levels, to monitor treatment in cases of iron overload." *Physics in medicine and biology*, vol. 45, no. 5, pp. 1387–96, 2000.

[18] K. Karimi, M; Marvasti, VE; Rasekhi, A; Kumar, PV; Bordbar, M; Moshiri, A; Hasanpour, P; Serajzadeh, "MRI Evaluation of liver concentration in patients with beta-thalassemia major," *Hepatitis Monthly2*, vol. 10, no. 2, pp. 149–150, 10.

[19] M. G. Bonetti, A. Castriota-Scanderbeg, G. M. Criconia, P. Mazza, M. Sacco, B. Amurri, and C. Masi, "Hepatic iron overload in thalassemic patients: proposal and validation of an MRI method of assessment," *Pediatr Radiol*, vol. 26, no. 9, pp. 650–656, 1996.

[20] E. Brittenham, GM; Farrell, DE; Harris, JW; Feldman, ES; Danish, EH; Muir, WA; Tripp, JH; Bellon, "Magnetic-susceptibility measurement of human iron stores," *The New England Journal of Medicine1*, vol. 307, pp. 1671–1675, 1982.

[21] P. Nielsen, R. Fischer, R. Engelhardt, P. Tondüry, E. E. Gabbe, and G. E. Janka, "Liver iron stores in patients with secondary haemosiderosis under iron chelation therapy with deferoxamine or deferiprone." *British journal of haematology*, vol. 91, no. 4, pp. 827–33, 1995.

[22] M. Berger, J. Hubbell, S. Seltzer, J. Chang, J. Coursey, R. Sukumar, D. Zucker, and K. Olsen, *NIST Standard Reference Database 8 (XGAM)*. NIST, PML, Radiation Physics Division, 1998.

[23] G. P. Williams, "Electron binding energies, in electron volts, for the elements in their natural forms," *X-Ray Data Booklet*, 2009.

[24] M. Haggstrom, "Layers of the epidermis," 2010.

[25] D. A. Bradley and M. J. Farquharson, "XRF and thein vivo evaluation of toxicological metals," *X-Ray Spectrometry*, vol. 28, no. 4, pp. 270–274, 1999.

[26] A. Al-Ebraheem, E. Dao, E. Desouza, C. Li, B. C. Wainman, F. E. McNeill, and M. J. Farquharson, "Effect of sample preparation techniques on the concentrations and distributions of elements in biological tissues using µSRXRF: a comparative study." *Physiological measurement*, vol. 36, no. 3, pp. N51–60, 2015.

[27] E. D. Desouza, I. A. Atiya, A. Al-Ebraheem, B. C. Wainman, D. E. B. Fleming, F. E. McNeill, and M. J. Farquharson, "Characterization of the depth distribution of Ca, Fe and Zn in skin samples, using synchrotron micro-x-ray fluorescence (SR-XRF) to help quantify in-vivo measurements of elements in the skin," *Applied Radiation and Isotopes*, vol. 77, pp. 68–75, 2013.

[28] M. Estevam and C. R. Appoloni, "Use of Portable X-Ray Fluorescence (PXRF) in vivo as an Alternative Technique for the Assessment of Iron Levels in Patients with Thalassemia and Hemochromatosis," 2013.

[29] M. J. Farquharson and D. A. Bradley, "The feasibility of a sensitive low-dose method for the in vivo evaluation of Fe in skin using K- shell x-ray fluorescence (XRF) The feasibility of a sensitive low-dose method for the in vivo evaluation of Fe in skin using K-shel," vol. 955, 1999.

[30] R. Gorodetsky, J. Sheskin, and A. Weinreb, "Iron, copper, and zinc concentrations in normal skin and in various nonmalignant and malignant lesions," *Int J Dermatol*, vol. 25, no. 7, pp. 440–445, 1986.

[31] D. J. Kalnicky and R. Singhvi, "Field portable XRF analysis of environmental samples," *Journal of Hazardous Materials*, vol. 83, no. 1-2, pp. 93–122, 2001.

[32] A. Longoni, C. Fiorini, P. Leutenegger, S. Sciuti, G. Fronterotta, L. Struder, and P. Lechner, "A portable XRF spectrometer for non-destructive analyses in archaeometry," *Nuclear Instruments and Methods in Physics Research, Section A: Accelerators, Spectrometers, Detectors and Associated Equipment*, vol. 409, no. 1-3, pp. 407–409, 1998.

[33] T. Radu and D. Diamond, "Comparison of soil pollution concentrations determined using AAS and portable XRF techniques," *Journal of Hazardous Materials*, vol. 171, no. 1-3, pp. 1168–1171, 2009.

[34] C. W. Roy, M. R. Gherase, and D. E. B. Fleming, "Simultaneous assessment of arsenic and selenium in human nail phantoms using a portable x-ray tube and a detector," *Physics in Medicine and Biology*, vol. 55, no. 6, pp. N151–N159, 2010.

[35] L. H. Nie, S. Sanchez, K. Newton, L. Grodzins, R. O. Cleveland, and M. G. Weisskopf, "In vivo quantification of lead in bone with a portable x-ray fluorescence system-–methodology and feasibility," *Physics in Medicine and Biology*, vol. 56, no. 3, pp. N39–N51, 2011.

[36] T. G. o. R. Q. E. i. R. Protection, "Relative Biological Effectiveness (RBE), Quality Factor (Q), and Radiation Weighting Factor (wR)," *Annals of the In-*

ternational Commission on Radiological Protection, vol. 4, no. 33, pp. 1–117, 2003.

[37] C. N. S. Committee, "Radiation doses," *Radiation Protection Regulations*, 2017.

[38] M. L. Cunningham, "A Mouse Is Not a Rat Is Not a Human: Species Differences Exist," *Toxicological Sciences*, vol. 70, no. 2, pp. 157–158, 2002.

[39] A. C. Pulla Reddy and B. R. Lokesh, "Effect of dietary turmeric (curcuma longa) on iron-induced lipid peroxidation in the rat liver," *Food and Chemical Toxicology*, vol. 32, no. 3, pp. 279–283, 1994.

[40] R. E. Anderson, L. M. Rapp, and R. D. Wiegand, "Lipid peroxidation and retinal degeneration." *Current eye research*, vol. 3, no. 1, pp. 223–7, 1984.

[41] M. J. Burkitt and R. P. Mason, "Direct evidence for in vivo hydroxyl-radical generation in experimental iron overload: an ESR spin-trapping investigation." *Proceedings of the National Academy of Sciences of the United States of America*, vol. 88, no. 19, pp. 8440–8444, 1991.

[42] E. I. Goldenthal, "A compilation of LD50 values in newborn and adult animals," *Toxicology and Applied Pharmacology*, vol. 18, no. 1, pp. 185–207, 1971.

[43] E. M. Johnston, S. H. Byun, and M. J. Farquharson, "Determination of optimal metallic secondary target thickness, collimation, and exposure parameters for X-ray tube-based polarized EDXRF," *X-Ray Spectrometry*, vol. 46, no. 2, pp. 93–101, 2017.

[44] E. D. Desouza, M. R. Gherase, D. E. B. Fleming, D. R. Chettle, J. M. O'Meara, and F. E. McNeill, "Performance comparison of two Olympus InnovX handheld x-ray analyzers for feasibility of measuring arsenic in skin in vivo - Alpha and Delta models," *Applied Radiation and Isotopes*, vol. 123, no. November 2016, pp. 82–93, 2017.

[45] K. Jacob, G. Vivian, and J. R. Steel, "X-ray dose training: Are we exposed to enough?" *Clinical Radiology*, vol. 59, no. 10, pp. 928–934, 2004.

[46] R. Parry, S. Glaze, and B. Archer, "The AAPM/RSNA Physics Tutorial for Residents Typical Patient Radiation Doses in Diagnostic Radiology," *Imaging & Therapeautic Technology*, vol. 19, pp. 1289–1302, 1999.